Naval Research Laboratory

Washington, DC 20375-5320

Histograms of Arecibo World Days Measurements and "Linear-H" Fits Between 1985 and 1995

D. J. MELÉNDEZ-ALVIRA
J. M. PICONE

E.O. Hulburt Center for Space Research
Space Science Division

O. A. KELLEY

George Mason University
Fairfax, VA

Q. ZHOU
M. P. SULZER

Arecibo Observatory
Arecibo, PR

November 30, 1998

19981231 019

DTIC QUALITY INSPECTED 5

REPORT DOCUMENTATION PAGE

1. AGENCY USE ONLY (*Leave Blank*)	2. REPORT DATE November 30, 1998	3. REPORT TYPE AND DATES COVERED NRL Memorandum Report	

4. TITLE AND SUBTITLE

Histograms of Arecibo World Days Measurements and "Linear-H" Fits Between 1985 and 1995

5. FUNDING NUMBERS

6. AUTHOR(S)

D.J. Meléndez-Alvira, J.M. Picone, O.A. Kelley,* Q. Zhou,** and M.P. Sulzer**

7. PERFORMING ORGANIZATION NAME(S) AND ADDRESS(ES)

Naval Research Laboratory
Washington, DC 20375-5320

8. PERFORMING ORGANIZATION REPORT NUMBER

NRL/MR/7640--98-8311

9. SPONSORING/MONITORING AGENCY NAME(S) AND ADDRESS(ES)

10. SPONSORING/MONITORING AGENCY REPORT NUMBER

11. SUPPLEMENTARY NOTES
*George Mason University, Fairfax, VA 22030
**Arecibo Observatory, Arecibo, PR 00613

12a. DISTRIBUTION/AVAILABILITY STATEMENT

Approved for public release; distribution unlimited.

12b. DISTRIBUTION CODE

13. ABSTRACT (*Maximum 200 words*)

This document presents histograms of "linear-H" model fits to electron density profiles measured with the incoherent scatter radar of the Arecibo Observatory in Puerto Rico during the World Days between 1985 and 1995. The linear-H model is a four-parameter analytical function, which is shown to fit the measured electron density profiles with better than 10% accuracy. The histograms show the distribution of the four model parameters as well as statistical measures of the model errors. In addition, the report presents histograms of electron temperature, ratios of electron and ion temperatures, and line-of-sight ion velocities at 589 km. The histograms characterize the ten years of Arecibo World Days, effectively showing a climatology of the actual ranges of both model and topside parameters.

14. SUBJECT TERMS

Incoherent scatter radar	Topside	Statistical distributions	Model errors
World Day	Peak height	Electron density profiles	
Ionosphere	Histograms	Peak density	

15. NUMBER OF PAGES

67

16. PRICE CODE

17. SECURITY CLASSIFICATION OF REPORT UNCLASSIFIED	18. SECURITY CLASSIFICATION OF THIS PAGE UNCLASSIFIED	19. SECURITY CLASSIFICATION OF ABSTRACT UNCLASSIFIED	20. LIMITATION OF ABSTRACT UL

CONTENTS

Histograms of Arecibo World Days Measurements and "Linear-H" Fits Between 1985 and 1995

D. J. Meléndez-Alvira, J. M. Picone
E. O. Hulburt Center for Space Research, Naval Research Laboratory, Washington, DC 20375
O. A. Kelley
George Mason University, Fairfax, VA 22030
Q. Zhou, and M. P. Sulzer
Arecibo Observatory, Arecibo, PR 00613

16-Nov-98

1. Introduction

Three decades of incoherent scatter radar measurements have greatly advanced ionospheric physics by providing accurate electron and ion densities, electron and ion temperatures, and ion velocities as a function of time and altitude. Reviews on incoherent scatter radar measurements and techniques were made by Burnside et al. (1991), Suvanto (1990), Mathews (1986), Sulzer (1986), Evans (1978), and Farley (1971). By now there are long term datasets in most of the incoherent radar observatories, harboring what can be termed as ionospheric climatology. This report presents frequency histograms covering ten years of incoherent scatter radar measurements at the Arecibo Observatory (18° 20' N, 66° 45' W, 50° magnetic dip) in Puerto Rico. The Arecibo measurements were made during the regularly scheduled World Days using the multi-frequency technique of Sulzer (1986) between October 1985 and May 1995 [Figure 1]. Over 140,000 Arecibo profiles were recently reanalyzed at the Observatory in order to benefit from improvements in numerical fitting of the measured incoherent scatter spectra. These improvements led to resolving O^+, H^+, and He^+ ions simultaneously in the measured spectra [González and Sulzer, 1996], and retrieving more accurate topside ion and electron temperatures [Sulzer and González, 1996].

The standard World Day mode at Arecibo records incoherent scatter spectra for altitudes between 144 and 627 km, in 38-km increments. Before 1985, the standard World Day program transmitted 300 μs pulses at 430.0 MHz. Since October, 1985, the program uses the multi-frequency technique of Sulzer (1986), phase modulating a 308-μs pulse and recording seven independent spectra per range gate. These are alternated with a 13-baud (4 μs per baud) Barker

coded pulse. In addition, 15 range gates per IPP (inter-pulse period) are recorded after September 1986, instead of 14, thanks to a faster array processor.

World Day observations between 1985 and 1990 are discussed by Burnside et al. (1991). Their 14-day period averages show solar cycle control of the height of the F2 layer peak height (zmax) and density (Nmax). Other studies summarize Arecibo ExB drifts [Fejer, 1996], electric fields [Ganguly et al., 1987], and meridional wind data [Harper, 1973]. This study presents a statistical summary or climatology of the Arecibo World Days in the NCAR-CEDAR database up to 1995. Specifically, we present frequency distributions of important observables such as peak density, peak height, electron temperature (T_e), the electron and ion temperature ratio (T_e/T_i), line-of-sight ion velocities, and H^+ and He^+ fractions. No published report we know shows long-term statistical frequencies of Arecibo measurements. The importance of the distributions is in quantifying the physically realizable values of the ionospheric state variables measured during World Days. Such information is also valuable in evaluating numerical or empirical models, geophysical events, and in planning and designing future sensor and experiments. Furthermore, the Arecibo electron density profiles are fitted using a four-parameter model, and the parameter distributions are presented.

2. The "Linear-H" Model

A model of the electron density profile is required to extract F2 peak height and density from the measured altitude profiles of electron density. This is because the relatively coarse altitude resolution (~38 km) may miss the actual peak height. In addition, noise can obscure the precise values of both the peak height and density. In the World Day program, absolute power calibration is provided by scaling the density profiles with foF2 measurements from the ionosonde on-site or the Ramey ionosonde some 40-km to the northwest. However, the ionosonde calibration is less frequent than the measurement interval of a few minutes per profile. The simplest way to extract the parameters at the peak is just to define the altitude with the largest electron density as zmax, with Nmax as the density at that height. The obvious drawback is that the actual peak may be located above or below the range gate of maximum electron

2

density. A popular approach is to fit with a function, such as a parabola, the three consecutive range gates centered on the largest electron density. The zmax and Nmax reported in the NCAR-CEDAR database are obtained by fitting the entire profile with cubic splines, an interpolation that goes through each data point. These methods are flawed in that they do not account for the ever-present noise, giving $\chi^2=0$. However, there is generally good agreement between the cubic-splines fitting and the Barker-coded profiles. The Barker-coded profiles have 600-m height resolution.

Our approach is to fit the measured electron density profile with a four-parameter Chapman-like function [Picone et al., 1997] or "linear-H" model, excluding range gates below 200 km. The Chapman layer representation [Chapman, 1931], and an altitude varying scale height are discussed by Rishbeth and Garriott [1969]. Other Chapman-like layers are discussed by Fox [1994]. We denote the model peak height and density as hmax and nmax, respectively, to distinguish them from the corresponding CEDAR database parameters zmax and Nmax, respectively. The function is similar to the three-parameter Chapman formula [Burnside et al, 1983; Anderson et al., 1985] but adds a fourth parameter, which defines the height-varying pseudo-scale height linear term, hence the name linear-H. The linear-H function is given by

$$Ne(z) \quad = \quad nmax \exp \left[\frac{1}{2} \left\{ 1 - z - e^{-z} \right\} \right] \tag{1}$$

where z(h) is the reduced height given by

$$z(h) = (h - hmax) / H_m(h) \tag{1a}$$

and $H_m(h)$ is the linear scale height parameter, given by

$$H_m = H_0 + H_1 (h - hmax) \text{ for } h > hmax \text{ and } H_m = H_0 \text{ for } h < hmax. \tag{1b}$$

The four parameter vector for the model is thus [nmax, hmax, H_0, H_1]. Numerical fits are made using Levenberg-Marquardt minimization of χ^2 [Picone et al, 1997], which accounts for

measurement noise. Two advantages of the linear-H function are simplicity --only four parameters are used to describe the profile-- and that the parameters are geophysically meaningful. The physical basis of the model is that the function is a solution to the ion continuity equation. Below we provide statistical measures of the quality of the resulting fits.

3. Results

3.1 Dataset

Table 1 summarizes the statistical properties of the linear-H fits to the Arecibo World Days between 1985 and 1995. The distribution of the daily F10.7 or 10.7-cm flux values corresponding to the Arecibo World Days considered here is shown in Figure 1. High solar activity is centered in the middle of the observing period during 1989-1992, with F10.7 index reaching 275. Low solar activity is found at the beginning and ending periods, with F10.7 values as low as 75 during 1985-87 and 1994-95. Since the median F10.7 is 133, the dataset contains more World Days in solar maximum than solar minimum. This small bias results from a data gap in the second half of 1991, as shown in Figure 2. Monthly coverage is irregular, as shown in Figure 3: March, May, and July are barely represented in the dataset with frequencies of less than 0.05 or 5% each. Most of the measurements were taken during the months of January, April, July, and during Fall. Local time coverage is, on the other hand, highly uniform, as shown in Figure 4. Antenna pointing, shown in Figure 5, is very uniform with a beam elevation of 15° off-zenith. As is typical of the World Day program, the beam is swung azimuthally, recording three profiles every four minutes during the 16 minutes needed for one 360° rotation.

The distribution of peak densities in Figure 6 shows large positive skew, with the most frequent bin, denoted by "mode", at 0.2×10^{12} m^{-3} (Table 1). Two histograms are shown: one for the nmax obtained with linear-H, another for the Nmax values directly from the NCAR-CEDAR database (obtained with cubic spline interpolation). The linear-H and splines histograms are very similar, though the CEDAR Nmax has mean and median which are 20% and 30% smaller than the corresponding linear-H values (Table 1). The reason for this is that the linear-H model has

4

distribution has slightly lower nmax values below about 0.4 x 10^{12} m^{-3} but a higher frequency of larger peak densities than CEDAR between 0.4 x 10^{12} m^{-3} and 2 x 10^{12} m^{-3}. Only 23 out of 9801 fits are larger than 3 x 10^{12} m^{-3}. The distribution includes both day and night measurements with the largest peak densities occurring in the afternoon [Burnside et al., 1991]. Using data from half of a solar cycle, Burnside et al. (1991) found Nmax to increase with increasing F10.7 values. Our data shows a similar trend.

The peak height distributions in Figure 7, on the other hand, show a broad and symmetric linear-H hmax distribution (solid line) with mode at 315 km, while the corresponding CEDAR (splines) distribution fluctuates considerably. The two distributions have similar statistics (Table 1). The mean hmax is 316 ± 51 km ("mean ± standard deviation") for the linear-H model; the CEDAR mean is 320 ± 49 km (Table 1). The median in the linear-H distribution is 317 km whereas the median in the CEDAR hmax is 316 km. The CEDAR distribution has two large frequencies at about 310 km and 365 km. The linear-H distribution can be fitted with a Gaussian function of amplitude 0.02, mean of 314.3 km, and standard deviation of 52.3 km. These parameters agree with those in Table 1 to better than 3 km, suggesting that the linear-H hmax is normally distributed unlike nmax (Fig. 6). The Gaussian is most accurate for hmax values above about 370 km while it overestimates the very low peak heights.

The highest F2 layer at Arecibo occurs prior to midnight, reaching 380 km [Burnside and Tepley, 1989]. The phase (i.e., local time) of highest hmax is also prior to midnight with the linear-H fits to the data. The lowest layer height occurs in the morning, reaching an average of 260 km [Burnside et al., 1991]. The extremes in the diurnal average of Burnside et al. fall within the standard deviation of the distribution. Our distribution is consistent with the scatter in the diurnal variation reported by Burnside et al., which can be as large as 100 km. They also found solar cycle variability to be larger than the seasonal variability. Our preliminary evaluation of the 1985-1995 fits gives results similar to those of Burnside et al. Our database has the advantage of greater sampling, particularly during high F10.7 values. Thus, the distributions in Figure 7 are dominated by diurnal, solar cycle and seasonal variations, in descending order of importance. Overall, the Arecibo F2 peak is rarely found above 400 km or below 230 km though peak heights below 200 km are less accurately determined. This is due to the large bottomside gradient in the

electron density caused by the higher loss rates, also known as the range-smearing problem that occurs when the pulse length is longer than the characteristic scale length of the medium.

3.2. Model and Data Uncertainties

A model fit should provide, in addition to the fit parameters and uncertainties ("errors"), a statistical measure of the goodness of fit. The distribution of the reduced-χ^2 values obtained in fitting the profiles with the linear-H model is shown in Figure 8; the calculation includes both measurement and model error covariance calculations as described by Picone et al. [1997]. Figure 8 shows the distribution of $\log_{10}$ of reduced χ^2, one value per fitted profile. The fits to the chosen $N_e(h)$ profiles are obtained by minimizing χ^2 with a modified Levenberg-Marquardt algorithm, as discussed by Picone et al. [1997]. Each profile fit is terminated when χ^2 changes by less than 1 part in 10^{-5} or upon reaching 200 iterations, whichever comes first. The distribution peaks at $\log_{10}\chi^2 = 0$ or $\chi^2 = 1$, indicating a good overall fit. A value of $\chi^2 = 1$ means that the residuals or deviations are equal to the random fluctuations expected from the measurements. The overall distribution has a mean of $\chi^2 = 1.15 \pm 6.09$ ($\log_{10}\chi^2 = 0.06 \pm 0.785$). This is the result of the model parameters chosen by the fitting algorithm, excluding fits with $|\chi^2| < 10^{-4}$. Values of χ^2 greater than 10 and smaller than 0.1 account for less than 16% of all the fits (Table 1); thus, 16% represents the nominal fraction of "outlier" fits. Therefore, most of the fits produce adequate values of χ^2. Too small χ^2 fits may indicate large or overestimated experimental uncertainties, while large χ^2 fits may indicate underestimated data uncertainties or a bad functional fit.

Another measure of the accuracy of the model fits is the distribution of the uncertainties in the data and fit parameters. By uncertainty, we mean a variety of statistical measures of error, such as the residual $(x - X)$ between the model (linear-H) parameter x and the corresponding data parameter X. Also, ΔX denotes the uncertainty in the CEDAR data while Δx denotes the uncertainty in the model (obtained from the diagonal element of the covariance matrix of the fit), normalized by either x or X. The quantity σ denotes the standard deviation, specifically $\sigma = \sqrt{(\text{variance})}$.

Figure 9 shows the relative model fit uncertainty in nmax, specifically, the fractional percentage uncertainty in the model peak density, Δnmax, given by

$$\Delta nmax = 100. \ \sigma(nmax) \ / \ nmax \qquad (2)$$

where σ(nmax) is obtained from the linear-H fit covariance matrix. The covariance matrix equation is given by equation (13) of Picone et al. [1997], and the variance is estimated using a formula similar to Eqn. (15) from that reference. The overall distribution looks like the sum of a Gaussian and a smaller skewed distribution (Fig. 9). The skewed distribution is not negligible since nearly 28% of the distribution has values above 4% though the low frequencies (below 0.002) indicate considerable spread. However, 85% of the Δnmax distribution is within 10% (Table 1). The "outlier" population (remaining 15%) is of the same size as the outliers in the nmax and hmax distributions (Table 1). The mode (most frequent value) in the distribution of the uncertainty in nmax (Equation 2) is nearly 2% (Fig. 9) with a frequency just below 2% also, using 200 bins. There are no negative values since σ (nmax) is positive definite. The median, which is less sensitive to outliers, is 2.4%. If Δnmax > 100% are excluded (13% of the distribution) the mean becomes 3% ± 5%. The precision in the model peak density is comparable to the typical uncertainty of the Arecibo incoherent scatter radar measurements of the peak.

The distribution of the uncertainties in the model hmax, Δhmax, shown in Figure 10, is analogous to Δnmax. However, Δhmax is about three times narrower distributed than Δnmax, and its mode is twice as frequent (Table 1). The median in Δhmax is 0.6%, or about 4 times smaller than the median in Δnmax. Both the Δhmax and Δnmax distributions have similar populations with values of 10% or less (Table 1). However, Δhmax is less skewed than Δnmax. Neglecting Δhmax > 100% (12% of the population), the mean becomes 1.4% ± 5.5%. Therefore, the linear-H uncertainties are lower for hmax than for nmax. In other words, the data provides a more precise determination of hmax than nmax. The model uncertainty in hmax is uniformly distributed in time while Δnmax peaks after dawn.

The differences between the linear-H and the splines models can be described by comparing the distribution of the residuals between the respective values of nmax and hmax. Figures 11 and 12 show the distributions of the percentage residuals, D, in peak density and height, respectively, as given by

$$D(x - X) = 100. (x - X) / X \qquad (3)$$

where x = linear-H fit of hmax or nmax, and X = CEDAR (cubic splines) zmax or Nmax, normalized by the corresponding CEDAR values. Zero-residual occurs when the linear-H and splines estimates are equal. The asymmetry and negative skew in the peak density residuals (Fig. 11) show a definitive bias between the two estimates. In particular, the linear-H peak density is lower than the splines estimate in 58% of all cases, a result also implied in Fig. 6. The bias or mean residual is -0.9 ± 4.5%; the median is also small and negative (Table 1). On the other hand, the two methods usually yield similar estimates. Values of $D(nmax\text{-}Nmax)$ fall outside ±5% in less than 10% of all cases, and outside ±10% in less than 3% of all cases (Table 1). In other words, the great majority of linear-H and the CEDAR database estimates are within 10% of each other. The "3σ" level of confidence of a normal distribution is at the residual level of ±10% since these account for nearly 97% of all comparisons.

The parameter $D(hmax\text{-}zmax)$ is the residual between the model and measured hmax, and is more normally distributed (Fig. 12) than $D(nmax\text{-}Nmax)$ (Fig. 11). There is a negative bias of –1%, which implies that the linear-H peak height is three km lower than the splines on average (Table 1). However, peak height estimates by the two methods are randomly distributed about the –1-km mean. Over 90% of the values of $D(hmax\text{-}zmax)$ are 5% or smaller. Therefore, the data and the linear-H fits agree to within 5% in well over 90% of the cases, well within the "2σ" or 90% level of confidence for a normal distribution. The linear-H estimate of hmax is somewhat more precise and accurate than its estimate of Nmax (Figs. 11-12). There is also a negative skew in the distribution, where, for example, the -5% residual is over six times more frequent than the +5% residual. The hmax (linear-H) is, therefore, more often smaller than zmax (CEDAR), a finding supported by Fig. 7. This difference peaks at mid-morning, so the linear-H value is smallest at that time (not shown). The model value is, on the other hand, largest at midnight.

The linear-H model is actually a representation of the electron density profile, not just the peak height and density. A measure of the overall accuracy of the linear-H fit to the measured electron density profile is the average of the altitudinal sum of the absolute deviations between the model and measured electron densities, normalized by the measured density. This average residual, B, is given by

$$B(n_e) = 100 \ (1/M) \ \Sigma \ |(n_e(j) - N_e(j))| \ / \ N_e(j) \qquad (4)$$

where $n_e(j)$ is the linear-H electron density at the jth range gate, $N_e(j)$ is the corresponding measured value, and M is the number of range gates (altitudes) in each profile. The sum in (4) is over all range gates fitted (i.e., at or above 200 km), and is always positive. The parameter B is the average magnitude of the residual of the model and measured electron densities in each fitted electron density profile. The closer B is to zero, the more similar are the model and measured $N_e(h)$ profiles. The quantity B measures how well a profile was fitted while the distribution measures how many profiles were fit with a particular B value. The distribution of B, shown in Figure 13, has a mode between 1% and 2%, and a plateau centered at 5%. The mean and standard deviation in the distribution of B are $5 \pm 23\%$, and the median is 3.6% (Table 1). The relatively large standard deviation is caused by the positive skew in the distribution, and a few large outliers. However, the cumulative frequency for $B > 20\%$ is less than 0.015 (1.5%). That is, less than 2% of all fitted profiles have an average residual of more than 20% (Table 1). If the distribution is truncated to $B \le 100\%$, the mean is unchanged but the standard deviation decreases to $\pm 5\%$. Inspection of Fig. 13 shows that over 69% of the values of B are smaller than 7%. Since 94% of all fits have values of $B \le 10\%$, the linear-H model fits the measured profiles with an accuracy of better than 10% at the "2σ" or 90% level of confidence for a normal distribution. The best fits, as measured with B, are achieved at night whereas the values of B near 6% occur in the morning (not shown). As expected, the linear-H model is most accurate at night when there is no E or F_1 layer.

There is an analogous parameter to B, but one based solely on the uncertainties of the measured electron density profile listed in the CEDAR database. This is the altitude-averaged percentage of the experimental uncertainty in $N_e(h)$ normalized by the measured electron density, $D(N_e)$, given by

$$D(N_e) = 100 \ (1/M) \ \Sigma \ \sigma(N_e(j)) \ / \ N_e(j) \tag{5}$$

where $\sigma(N_e(j))$ is the uncertainty in the measured $N_e(j)$ at the jth range gate, summed over all the range gates; the other quantities are as defined in equation (4). Thus, $D(N_e)$ measures the average experimental uncertainty of all profiles. This quantity is readily compared to the average fit residual B (Fig. 13). Similar distributions of B and D would indicate similar levels of precision in the linear-H and measured electron density profiles. Such comparison (Table 1) indicates that the accuracy of the linear-H model is similar to the average experimental uncertainty since the mean, median, and standard deviation of B and D are nearly identical (Table 1). That is, the model fit is as accurate as the data is precise. The distributions are different in that D is nearly Gaussian whereas B is skewed.

The two distributions have identical cumulative frequencies: over 98% of the distributions are 20% or less in value. Less than 10% of the D distribution has values larger than 10%, a figure comparable to that of the outliers in the model fits. The D distribution has, however, more and larger outliers than the B distribution. If, on the other hand, profiles with $D > 100\%$ are ignored, the mean becomes $5.6 \pm 4.3\%$ which is just about equal to the median and the corresponding mean of the $B \leq 100\%$ distribution ($5 \pm 5\%$). Therefore, the uncertainties in the model and measured profiles are similar though their distributions have different shapes.

The distribution of the difference in the previous two measures, $B - D$, is symmetric and Gaussian-like, as seen in Figure 15. This can be interpreted as the distribution of the average difference in the uncertainty between the linear-H and measured electron density profiles. The difference is positive when data errors dominate, and negative when linear-H errors dominate. Values greater than $\pm 100\%$ have a cumulative frequency of less than 0.0004. The mean of the

distribution becomes -1 ± 6% if only differences within ±100% are counted, with median of -1.4% (Table 1). Therefore, the model and data uncertainties are within a few percent of each other, with slightly larger overall data errors. Moreover, 98% of the distribution is within ± 20%, 94% is within ± 10%, and 71% is within ± 5%. Less than 5% of the truncated distribution falls outside of ± 10%.

Each electron density profile has a vector of absolute residuals, F, normalized by the data, given by

$$F(h) = 100 \ |(n_e(h) - N_e(h))| / N_e(h) \qquad (6)$$

where $n_e(h)$ is the linear-H fit to the measured electron density at height h, $N_e(h)$. The median of each array of F contributes one value to the distribution of Figure 16. The median of F may be regarded as the median of the terms in the sum of B (Eqn. 4). That is, $B = \Sigma F$, where the sum is over the range gates of a given profile. The most frequent value of F is smaller than 1%, and the distribution is narrow (Table 1). Few profiles have median values of 10% or higher; their cumulative frequency is less than 0.05. Over 25% of the profiles in Fig. 16 have a median F between 0% and 1%. The distribution of medians of F is consistent with the magnitudes and mean values of the distributions in D and $(B - D)$. An appreciable number of large median values, not seen in Figure 16, would denote asymmetrical or strongly skewed distributions.

The minimum uncertainty of each measured profile as a fraction of the linear-H density, C, is given by

$$C = MIN \ [\sigma(N_e) / n_e] \qquad (7)$$

where $\sigma(N_e)$ is the array of uncertainties in the measured electron density profile (CEDAR database), and n_e is the linear-H electron density profile fit. The distribution of C, shown in Figure 17, is the combination of a near-zero spike, a symmetrical Gaussian-like function, and a small positive skew. The spike is a consequence of the relatively large distribution of errors smaller than 0.5%. There is a secondary broad peak at about 2%, with a cumulative frequency of

0.05. The mean of the distribution is $2.2 \pm 1.5\%$, and the median is 2%. Moreover, 99.7% of C are within 10%, and 96.6% is within 5%. Therefore, the most frequent minimum experimental uncertainty is several orders of magnitude smaller than the linear-H density. The C distribution is narrower than that of the average profile uncertainty (Fig. 13). Nearly half of the measured profiles have values of C smaller than 2%.

The statistical measures show that the linear-H model is accurate to within 5% level in well over 67% of the fitted profiles, and accurate to within 10% in at least 90% of the profiles. An examination of the remaining model parameters in (1) is in order. Whereas the model parameters nmax and hmax define the magnitude and location of the peak electron density, H_0 and H_1 define the height variation or profile shape. These parameters are deemed useful in and of themselves given the demonstrated accuracy of the linear-H model fits.

3.3. Model Profile Shape Parameters H_0 and H_1

The parameters H_0 and H_1 are related theoretically to neutral temperature and its altitude variation, respectively, though, strictly speaking, they are numerical parameters. The sum $H_0 + H_1$ represents, in theory, the atomic oxygen scale height $H = kT(h) / Mg$, where M is the mass of atomic oxygen, T(h) is the neutral temperature at height h, and g is the acceleration of gravity. More precisely, $H_0 + H_1$ is an effective or pseudo-scale height usually taking values consistent with an atomic oxygen scale height. The parameter H_0 is associated with the scale height near the F2 peak while H_1 is the average height gradient above the peak (Eqn. 1). As fit parameters, H_0 and H_1 can have whatever values are assigned to them in order to minimize χ^2 while matching the shape of the measured profile. The parameter H_0 is on the order of 50 km, as seen in Figure 18. This value corresponds to the atomic oxygen scale height of a typical thermospheric neutral temperature of 1000 K. The distribution of values of H_0 in Figure 18 has a broad peak at about 50 km, and a spike at 20 km. About 85% of the H_0 values forming the spike at 20 km are for F10.7 values of 100 or less. In other words, the spike is largely due to narrow profiles during solar minimum. There are values of H_0 as high as 120 km and as low as 15 km, for a six-fold spread. The mean in $H_0 = 51 \pm 16$ km, and the median is 50 km (Table 1). The extreme values are probably less representative of an actual scale height.

The spread of values in Fig. 18 represents the variability of electron density profile shapes since H_0 controls the altitudinal change of the linear-H profile, particularly below and just above hmax. The distribution of H_0 can be regarded as a proxy for the distribution in the neutral temperature, T, since the scale height is directly proportional to T. Thermospheric temperature increases with increasing F10.7 by over 50% [Hedin, 1987]. Since the distribution covers both large and small F10.7 values (Fig. 1), some of the larger values of H_0 are due to the increased solar heating of the upper atmosphere during solar maximum conditions. The average time variation in H_0 (not shown) peaks in the late afternoon, consistent with the measured variation [Hedin, 1987]. However, there is another peak just before dawn, which is also the time when H_1 is largest (not shown). The pre-dawn peak is indicative of the fact that H_0 and H_1 are model parameters, taking on large magnitudes at a time when the electron density profile broadens as a result of low density. This low density is due to the cumulative effect of recombination in the bottomside and diffusion from above, which results in a broad-peaked profile shape.

The high accuracy of the linear-H model is largely due to the fourth parameter, H_1. This parameter can be interpreted as the average altitude gradient in the pseudo-scale height above the F2 peak height. The parameter H_1 distinguishes the linear-H model from previous formulations based on the Chapman profile function [Anderson et al., 1987; Burnside et al., 1983]. Along with H_0, the parameter H_1 controls the shape of the profile above the F2 peak; however, $H_1 = 0$ below the F_2 peak. The units of H_1 are km per km. Figure 19 shows that the distribution of $\log_{10} H_1$ is skewed negatively. The mode of the $\log_{10} H_1$ distribution corresponds to H_1 of about 6 km per 100 km (Table 1). The parameter H_1 peaks at about 8 km per 100 km around 08 AST, and reaches its minimum in the early afternoon (not shown). About 18% of the profiles have H_1 values below 1 km per 100 km. The mean gradient of 4 km per 100 km gives the necessary flexibility for the linear-H model to fit the $N_e(h)$ profiles with a mean accuracy of $\pm 5\%$ (Fig. 13, Table 1).

The fractional uncertainties in H_0 and H_1 are distributed as shown in Figures 20 and 21, respectively. The uncertainties are obtained from the diagonal elements of the model covariance for each parameter, using equation (13) of Picone et al. (1997). Two thirds of the $\sigma(H_0)/H_0$

13

distribution (Fig. 20) fall within the 6% level. The $\sigma(H_0)/H_0$ distribution peaks at between 2% and 3% with 86% of the fits within 20%. Uncertainties larger than 100% have a cumulative frequency of less than 0.13 (13%), and 79% of the H_0 uncertainties are 10% or less. The mean becomes $5 \pm 5\%$ if only profiles with uncertainties within 100% are counted (Table 1). The percentage uncertainty in H_1 (Fig. 21), on the other hand, has an unusually flat distribution, with a peak of less than 1% at a rather high frequency (Table 1). In contrast to H_0, over 94% of the uncertainties in H_1 are 100% or less. The mean decreases to $19 \pm 19\%$ if the latter sub-population is used. Over two thirds of all values fall within the 23% uncertainty level. There is a greater range of uncertainties in $\sigma(H_1)/H_1$ than in $\sigma(H_0)/H_0$, which reveals a lower sensitivity of the data to H_1 in the model. However, the average model uncertainties (Figures 13 and 14) indicate that the overall accuracy of the model is better than that shown by the distributions of errors in H_0 and H_1 alone.

3.4. Distributions in the Topside Ionosphere at 589 km

There is considerable interest in a better understanding of the topside region above the ionospheric F_2 layer. Much of this arises from the need to improve total electron content (TEC) and light ion models. There is capability to detect light ion fractions with the Arecibo incoherent scatter radar. The reanalysis of the 1985-1995 World days applied this capability, yielding H^+ and He^+ densities (actually, the spectral fits provide ion fractions). Since the standard World Day can reach as high as 680 km, we chose the range gate 589 km as a representative altitude at which to evaluate the measured distributions of ion fractions as well as electron and ion temperatures. One limitation of the multi-frequency technique of Sulzer (1986) is that the bandwidth is reduced, compared to a single-frequency, in order to sample seven simultaneous spectra. The reduced bandwidth can limit the detection of large H^+ fractions since these produce frequency-broadened spectra. The broadened spectra can bias the ion temperature determination since both affect the shape of the spectrum in a similar way. As will be seen, the H^+ fraction distribution at 589 km shows relatively low fractions. However, some of the measured ratios of electron and ion temperature (T_e/T_i) are less than unity, suggesting that some of the H^+ fractions in the CEDAR database could be underestimating the actual fractions. Thus, the fractions and the temperatures are related by the similarity of their incoherent scatter radar spectra.

14

We present the first long-term distribution of T_e at Arecibo, shown in Figure 22. The F region electron and ion temperatures are important in determining the energy budget, the electron and ion scale heights, and in understanding the overall dynamic behavior. The distribution is skewed towards higher temperatures, exceeding 3000 K with a cumulative frequency of 0.05. However, 99.1% of the distribution is found below 3500 K. The largest and smallest temperatures at the 0.01 level are 3400 - 3500 K and 500 - 600 K. Thus, T_e varies by as much as a factor of five at the 1% frequency bin. The overall low frequency levels indicate that the ionospheric electrons at this altitude occupy a wide range of accessible thermal energies. This is in agreement with the significant scatter in T_e found by Mahajan (1967) and Kohnlein (1981).

The electron temperature exhibits a bimodal distribution at 589 km, with two broad peaks separated by about 800 – 900 K, beyond the range of the standard deviation. This bimodal distribution is due to two factors. The first is the diurnal variation in which nearly all of the temperatures lower than 1500 K are nighttime values. The second is that T_e varies with changing solar activity [Grebowski et al., 1993]. We find that the nighttime T_e increases with solar activity whereas the daytime T_e decreases with increasing solar activity (F10.7). The decrease with increasing F10.7 is consistent with both the electron density at 589 km and the peak density increasing with higher solar activity. In summary, the topside electrons are hotter at night during high solar activity but are cooler during daytime whereas the low F10.7 topside is colder at night but hotter during daytime. While all local times are sampled equally, about 20% of the temperatures during low solar activity were measured during winter.

The ratios of electron to ion temperature at 589 km, T_e/T_i, are shown in Figure 23. There is a broad maximum between 1.0 and 1.3, and a mean of 1.3 ± 0.4; the median is 1.22 (Table 1). A ratio of one would be expected with frequency of 0.5 since $T_e = T_i$ at night, and nearly half of all the measurements are nighttime (Fig. 4). Carpenter and Bowhill, [1971] found that T_e/T_i need not be one throughout the entire night, particularly during winter. Thus, the distribution need not be evenly distributed about $T_e/T_i = 1$. The cumulative frequency or population for $T_e/T_i > 1.1$ is larger than 0.6; for $T_e/T_i > 1.3$ the frequency is about 0.4. The largest T_e/T_i ratios occur typically during sunrise when the plasma is least dense and efficiently heated by photoelectrons, and in

daytime when photoelectron and plasmaspheric heating rates are greatest. At 589 km, $T_e/T_i = 2$ is seen with a frequency of 0.03 while values of $T_e/T_i > 2$ have a cumulative frequency of close to 0.05. However, T_e/T_i ratios greater than two can be regarded as outliers.

Values of $T_e/T_i < 1$ are a consequence of the freedom of the non-linear least squares fit of the incoherent scatter spectra to assign whatever T_e/T_i ratio best fits the measured spectrum. These low ratios, however, are unphysical since there is no mechanism allowing the more massive ions to become hotter than the electrons. Therefore, $T_e/T_i < 1$ values are an artifact of the fitting process of noisy spectra, though as many as 13% of the ratios are less than one. Note that both day and night values of T_e/T_i are shown in Fig. 23. Fits with $T_e/T_i < 1$ generally are found at night but account for only 13% of the distribution. The temperatures and the H^+ and He^+ fractions are related in the radar spectrum [Evans and Louwenthal, 1964]. Low levels of He^+ in the spectrum may be confused for high ion temperatures, resulting in too low a T_e/T_i ratio. However, a cursory examination does not reveal any abnormality in the light ion fractions correlating with $T_e/T_i < 1$. In addition, the spectral reduction assumes all ions have a common temperature. Recent work by Sulzer and Gonzalez (1996) shows distinct O^+ and H^+ temperatures at Arecibo, and these improve upon the spectral fits. Two-temperature fits were not done with the World Day dataset.

The distribution of the measured electron density at 589 km, N_e(589 km), is shown in Figure 24. A comparison of the N_e(589 km) and nmax distributions (Fig. 6) shows that the former has a higher (more concentrated) peak than the nmax distribution. The mean in N_e(589 km) is 2.3 ± 2.5 x 10^{11} m^{-3}, with frequency of about 0.01, whereas the mean of the nmax distribution is 9.8 ± 6.7 x 10^{11} m^{-3}, with similar frequency as N_e but four times larger bin size (Table 1). A smaller bin size decreases all the frequencies, resulting in a less frequent peak value. The N_e(589 km) distribution is more peaked than nmax in spite of the smaller bin size. Another way to examine the spread is by comparing the standard deviation as a fraction of the mean in the distribution: 1.09 for N_e versus 0.68 for nmax (Table 1). The topside density is more spread than nmax. The N_e distribution is strongly skewed positive though there are only 156 values larger than 10^{12} m^{-3} out of 9801 sampled. Thus, there are very few outliers but a greater spread of electron densities at 589 km than at the F_2 peak (Nmax). Unlike T_e (Fig. 22), however, the Ne distribution shows

no bimodality. This suggests that the bimodality in Te does not require a corresponding bifurcation in the electron density. The skewness in N_e, however, is large enough to account for the bifurcation in T_e(589 km).

The H^+ fraction distribution at 589 km, shown in Figure 25, is weakly bimodal with peaks separated by just a few percent: below the 1% fraction and just above 2%. The distribution is also skewed positive, like N_e(589 km) (Fig. 24). The most probable H^+ density can be estimated by multiplying the modes of H^+ fraction and N_e at 589 (Table 1) or about 0.75×10^9 m^{-3} (750 cm^{-3}). The individual bin frequencies are rather low: the H^+/Ne = 6% level has a frequency of only 0.02. The mean, $<H^+/Ne>$ = 0.13 $\pm$ 0.21, has a frequency of only 0.02, and the median fraction is just 0.04. Proton fractions of 15% and higher have a cumulative frequency of 0.23 whereas fractions greater than 50% (i.e., 0.5) have a cumulative frequency of 0.07. Overall, H^+ fractions between the 0.10 and 0.25 fractions are about equally likely. Higher proton fractions are much less frequent in the distribution. The skew in the distribution is due to the variability of the H^+ density in the topside, which varies with local time [Tepley and Kerr, 1987; Ho and Moorcroft, 1971], magnetic activity [Tepley and Kerr, 1987], season [Tepley and Kerr, 1987; Prasad, 1968], and, solar cycle [Bailey et al., 1982; Evans and Holt, 1978; Prasad, 1968].

Modeling [Bailey et al., 1982] shows that the H^+ fraction is most sensitive to changes in the neutral hydrogen density, which itself varies with solar cycle by as much as a factor of two [Tinsley, 1978]. At a fixed altitude, H^+/N_e increases during solar minimum since neutral hydrogen is more abundant than during solar maximum conditions at all latitudes [Kutiev et al., 1980]. Since H^+ is produced primarily by charge exchange between O^+ and H, the large abundance of hydrogen in solar minimum results in a greater proton fraction. However, diurnal changes in neutral hydrogen can be just as large. Thus, the flat portion of the H^+/N_e distribution contains both solar cycle and diurnal variations. In addition, the cumulative frequency of the 50% fraction or higher is of only 0.07. This low frequency suggests that the O^+--H^+ transition height is rarely found at 589 km or that the multi-frequency technique is limited in its ability to sample high proton fractions. The transition height can be as low as 475 km at night at Arecibo [Moorcroft, 1969; Prasad, 1968; Carlson and Gordon, 1966]. However, such low transition heights are generally found in the early morning near 0400 AST during solar minimum winter.

Also, OGO 6 [Kutiev et al., 1980] and AE E satellite [Gonzalez et al., 1992] measurements, as well as constrained incoherent scatter radar measurements at Arecibo [Erickson and Swartz, 1994], find the transition height generally above 600 km.

The He^+/N_e distribution, shown in Figure 26, has a large mode between 0% and 0.5%, unlike H^+/N_e. Low He^+ fractions are expected from other observations and modeling [Bauer, 1966; Prasad, 1968; Moorcroft, 1969; Bailey and Sellek, 1990; Hoegy et al., 1991; Gonzalez et al., 1992], and from the fact that neutral helium is less abundant than neutral hydrogen in the thermosphere and exosphere. Even the recently discovered He^+ bulge at Arecibo does not appear to exceed the 25% fraction [Gonzalez and Sulzer, 1996]. The mean of the entire distribution, $<He^+/Ne> = 0.03$, occurs with frequency of less than 0.05; the standard deviation of 0.09 is three times the size of the mean. The He^+ distribution is more narrowly peaked than that of H^+, so the two are quite different. Besides the mode, the next bin is about 10 times less frequent than the mode. This is due to the large number of "zero" fractions in the distributions (the median is 0.0000). A zero fraction does not mean zero He^+; instead, the actual fraction is too low or too high to be resolved in the radar spectral fits. The ion fraction distributions at 589 km show that: (i) He^+/Ne is generally smaller than H^+/Ne; (ii) both are skewed positive; and, (iii) He^+/Ne has lower frequencies beyond 10%.

The difference in the two distributions can be explained by the difference in the production and loss processes. Production of He^+ is largely due to photoionization (by solar EUV photons below 50.4 nm) at high altitudes whereas the loss rate peaks at low altitudes. Above the F_2 layer, the loss rate is small since there is little N_2 for He^+ to recombine. The largest He^+ fraction and density occurs at night due to inflow of He^+ from the plasmasphere. Modeling by Bailey and Sellek (1990) shows that $He^+/H^+ > 1$ at 500 km prior to sunrise in the L=1.8 flux tube during solar minimum equinox. The distributions here obtained provide some support for the possibility of equal fractions and concentrations: the 10% fraction has roughly equal probability for both ions. Of course, that does not establish coincidence, and, in an aggregate view, large He^+ fractions have lower frequencies than the corresponding H^+ fractions. The experimental uncertainties in the two ions are not equal for the same fractional values obtained from fitting the radar spectra (the He^+/Ne uncertainties are generally higher). Another difference, discussed

18

previously, is the small negative bias present in the He^+ distribution, which is an artifact of the fitting process that occurs with very noisy spectra when a common ion temperature is assumed. The bias is removed by allowing individual ions to have separate temperatures, as done by Sulzer and Gonzalez [1996]. There is not enough frequency bandwidth in the World day spectra to do multiple ion temperature fits.

The Arecibo World Days measured the radial (line-of-sight) ion velocity component as a function of altitude and beam azimuth. The radial speeds are used in obtaining the vector ion velocity and the ExB-drifts of the plasma [Behnke and Harper, 1973; Sulzer, 1986; Burnside et al., 1987; Fejer, 1993]. A single altitudinal profile of radial speeds is obtained at each azimuth position for a total of 12 profiles every 360° swing of the radar beam. The radial speeds at 589 km have a broad but symmetric distribution, shown in Figure 27, centered at zero velocity, with mean of -4 m s^{-1} (Table 1). The mean becomes -0.09 ± 31 m s^{-1} if only velocities within ± 100 m s^{-1} are considered, which comprise 95% of the population. The median in either case is zero velocity. There is no net plasma flow across 589 km on average, and positive and negative velocities are about equally probable. The large variability is evidenced by the broad wings in the distribution. There are certainly periods of net plasma transport in or out (down or up) but these are balanced in the long-term.

That the radial speed is a measure of net plasma motion across the 589 km boundary is both intuitive and formal. The line-of-sight velocity at height z, azimuth ϕ (measured counter clockwise from magnetic east), and zenith angle θ, v_r, is given by

$$v_r(z, \theta, \phi) = \sin\theta \,[\, v_s \sin\phi + v_e \cos\phi \,] + v_z \cos\theta \qquad (7)$$

where v_s is the horizontal ion velocity along the magnetic southward direction, v_e is the eastward ExB drift velocity component, and v_z is the vertical ion drift component due to vertical winds and given by

$$v_z = u_z \sin I \qquad (8)$$

19

where u_z is the vertical wind component, and I is the magnetic inclination angle. The southward ion drift, v_s, is given by

$$v_s = v_L \cos I - v_{\perp N} \sin I \tag{9}$$

where v_L is the parallel ion velocity (positive up along the magnetic field line), and $v_{\perp N}$ is the ExB-drift in the perpendicular-north direction. The parallel ion velocity contains the influence of ambipolar diffusion [Schunk and Walker, 1970], which, along with meridional neutral winds, drive plasma motions along the field line. Plasma motions along the radar line-of-sight are the sum of these velocities which, with the possible exception of vertical neutral winds, are present with varying magnitudes [Burnside et al., 1981]. A downward radial velocity arises from either a downward parallel drift, or a downward ExB-drift component, or a linear combination. Zonal ExB-drifts may cause radial velocities since there is a component along the line-of-sight whenever the beam points away from the magnetic meridian. The zonal drift, however, does not move plasma vertically. Zonal drifts will bias the radial distribution only if there is a non-zero zonal gradient in the zonal ExB drift. A bias can be also caused by a substantial change in the electric field during the beam swing (16-min).

The fact that the distribution is symmetrical about zero with near zero median implies that the zonal gradient is near zero or constant on average. According to Equation (8), a non-zero but constant zonal gradient induces a radial velocity when the beam points east but an equal and opposite component occurs with the beam in the western azimuth sector. The resulting components contribute equal positive and negative velocities but do not bias the azimuthal distribution. Only actual vertical velocities can generate a bias or moment in the distribution. Therefore, the zero bias cannot be caused by zonal gradients in the zonal drift, and the distribution of v_r is evidence of no net vertical plasma transport across 589 km over long time averages.

3.5. Ap Index

The level of geomagnetic activity in the dataset can be seen in the distribution of the Ap index, shown in Figure 28. The Ap index is a global average of the eight daily values of ap, which is the K index converted to a linear scale. The average is made over all the stations reporting K values, located mostly in the northern hemisphere. The Ap index ranges between 0 and 400; $Ap \leq 15$ ($Kp \leq 3$) denotes generally quiet conditions, whereas $Ap \geq 48$ ($Kp \geq 5$) denotes disturbed conditions. Most of the data has $Ap < 20$; the mode is 6, and the median is 11. The mean Ap is 14 ± 12, with frequency of 0.06. Values of $Ap > 27$ ($Kp = 4$) have a cumulative frequency of less than 0.04. Therefore, less than 4% of all the World days occurred during Ap values corresponding to geomagnetically disturbed conditions. Disturbed conditions may account for 4% frequency level effects in the distributions.

4. Summary and Conclusions

We present an "ionospheric climatology" comprised of histograms of 10 years of World Day measurements obtained with the Arecibo incoherent scatter radar as stored in the NCAR-CEDAR database. In addition, we compare the linear-H and splines model fits to the measured electron density profiles, the latter model being the one used in obtaining the peak height and densities in the CEDAR database.

1. About 55% of the observations correspond to solar 10.7-cm flux of 120 and higher. All local times were sampled equally (to within 20%) in the distribution of about 140,000 profiles obtained by pointing the beam at an elevation angle of 75°.

2. Model fits to the measured electron density profiles in the database were made using the four-parameter linear-H model consisting of F2 peak density (nmax), height (hmax), scale height (H_0) and linear scale height gradient (H_1). As many as 11,440 profiles were fitted, 90% with better than 10% accuracy on average. Thus, the linear-H model is accurate and precise to within 10%. The model accuracy in fitting measured electron density profiles matches the experimental uncertainty of 10% at the "one-sigma" level or higher. The four-parameters of the linear-H model retain physical meaning, although the fitting procedure treats them as purely numerical parameters.

3. Both the model and measured (cubic-splines) peak density distributions are very similar. Overall, the linear-H model peak densities below about 0.3×10^{12} m^{-3} are lower than those in the CEDAR database. Above this values, the linear-H peak densities are up to 20% to 30% higher, as seen by comparing the mean and medians (Table 1) of the distributions of the peak densities from linear-H and from the CEDAR database (Fig. 6). A more precise measure of this bias is seen in the distribution of residuals between the linear-H and database peak densities, which shows that negative residuals are more frequent than positive residuals (Fig. 11).

4. The linear-H distribution of peak heights is highly Gaussian. The distribution of peak heights obtained with splines, on the other hand, "fluctuates" about the corresponding linear-H distribution (Fig. 7), as expected from the fact that the splines do not account for measurement noise. The mean in the CEDAR peak height (zmax) is 320 ± 49 km whereas the linear-H peak height (hmax) is 316 ± 51 km; the corresponding medians are 317 and 316 km, respectively (Table 1). Therefore, the linear-H peak height is a few km lower than the splines zmax. In fact, the model underestimates zmax by about 1 km on average as seen from the mean and median of the distribution of residuals between the linear-H and CEDAR database values (Fig. 12). Nearly 68% of that distribution has negative residuals, confirming that the linear-H hmax is smaller than the CEDAR database value, obtained using a splines fit. In general, the linear-H model provides slightly lower peak height and densities than a splines fit.

5. The (reduced) χ^2 of the linear-H fits to the measured electron density profiles are distributed about one, which is the value expected of optimal fits. The distribution of $\log_{10}\chi^2$ is a broad Gaussian with standard deviation of ± 6 about a mean of 1.15, with 84% of the fits having χ^2 values between 0.1 and 10. A broad distribution can result from a pseudo-random or partial bias in the uncertainties assigned to the data.

6. The model precision in both peak density and peak height is within 10% in about 85% of the fits. The linear uncertainties in hmax are more narrowly distributed than nmax, as seen by comparing Figures 9 and 10. The fact that these errors have normal distributions preclude any significant model bias in the calculated variance.

7. The linear-H peak density (nmax) is within 10% of the CEDAR database values (Nmax) in over 96% of the fits, and within 5% in over 80% of the fits. The model underestimates the Nmax values obtained with splines by less than 1% on average, as seen by the distribution of the residuals between the model and measured peak densities (Fig. 11). Negative residuals are cumulatively more frequent, as seen from median and mean values of nearly –1%, and from the negative skew in the distribution.

8. The linear-H hmax is within 10% of the CEDAR values in about 98% of the fits, and within 5% in over 90% of the fits. The distribution of (normalized) peak height residuals (Fig. 12) is narrower than the corresponding peak density residuals (Fig. 11). The median of the distribution of residual is -1.2%, a slight underestimation by the linear-H model. The linear-H peak height and densities have similar accuracy, with virtually all residuals within ±10%.

9. The overall accuracy of the fits to the measured electron density profiles is evaluated from the distribution of the average absolute residual for each profile, as a fraction of the measured density (Fig. 13). By this measure, the linear-H profiles are well within 10% of the data in 94% of the fits, and within 5% in 66% of the fits. The linear-H model, therefore, fits the measured electron density profile with high accuracy (10% or better). The model accuracy is comparable to the average precision of the measured density profile (Fig. 14), which is within 10% in 89% of the profiles, and within 5% in 56% of the profiles. The median experimental precision is larger (4.6%) than linear-H (3.6%) by only 1%. Therefore, the model and the data have nearly identical accuracy and precision. Furthermore, the distribution of the difference between the linear-H residuals and the experimental uncertainties, also the difference of the previous two errors, shows that 94% of all the fits are within 10% of the experimental precision, and 71% of the profiles are within 5%. Therefore, the average linear-H residual is within 10% of the measured profile error.

10. The linear-H model parameter H_0 takes on values consistent with those expected from the atomic oxygen scale height near the F_2 peak, namely a mean, median and mode of about 50 km with a standard deviation of 16 km. The H_0 distribution can be regarded as a proxy for the neutral temperature near the peak, since the atomic oxygen scale height is directly proportional to the temperature. The most frequent uncertainty in H_0, as well as the median

uncertainty, is 4%; also, 79% of the uncertainties are within 10%. Furthermore, low values of H_0 of 20 km occur mostly for F10.7 values of 100 or less. The distribution of the precision in H_0 is similar to the average electron density profile error (Figs. 20 and 14).

11. The fourth parameter in the linear-H model, H_1, is the average linear altitude gradient, which modifies the pseudo-scale height H_0 and the electron density profile shape above the F_2 layer height. About 82% of all the model profiles have H_1 values greater than 0.01 scale heights per km (Fig. 19). The average gradient in the model scale height is 6 km / 100 km (Table 1). Therefore, the linear-H model implies non-zero scale height, and temperature, variation with altitude above the F_2 peak. The mode in the distribution of the precision in H_1 is less than 1% though the distribution is strongly skewed positive, with 66% of the errors within 23%. Over 94% of the errors are of 100% or less. The model assigns large errors to H_1 even when the overall fit uncertainties are small. Moreover, the skew in the H_1 precision contrasts with the more symmetrical distribution of the precision in H_0 (Fig. 20).

12. The electron temperature at 589 km has a strong bimodal distribution, which is consistent with solar cycle and local time dependence. The histogram peaks are separated by about 900 K and peak-to-valley frequency ratios of almost a factor of three. The database shows 99% of the T_e distribution falling below 3500 K. The T_e/T_i ratio at 589 km (Fig. 23), on the other hand, has a unimodal distribution with a peak at $T_e/T_i = 1.03$. A single T_e/T_i peak suggests that the ion temperature is also bimodal, following the electron temperature closely. Values of $T_e/T_i < 1$ appear in 13% of the distribution but these are unphysical, and due to the freedom afforded to the radar spectral fits. The topside electrons are hotter at night during high solar activity but are cooler during daytime, whereas the low F10.7 topside is colder at night but hotter during daytime.

13. The electron density at 589 km is unimodal, unlike the electron temperature. The distribution is flat between 0.4×10^{12} and 1×10^{12} m^{-3}. The density at 589 km has a stronger (more frequent) mode than the peak density (Fig. 6), which suggests a different variability occurs in the topside electron density. On the other hand, the spread of densities at 589 km is larger than nmax. As a fraction of the mean, the standard deviation at 589 km is about 60% larger than the standard deviation in nmax. Therefore, there is a wider spread of topside densities in

Ne than in nmax though the topside distribution is more sharply peaked. The bimodality in the electron temperature (Fig. 22) is not seen in the electron density.

14. The light ion (H^+ and He^+) fractions at 589 km are skewed positive. The proton fraction distribution is weakly bimodal, with a peak of less than 1% and another at 2.5%. The most probable H^+ density is 7.5 x 10^9 m^{-3} (750 cm^{-3}). Proton fractions of 0.25 (25%) and higher occur in 16% of the data while fractions between 10% and 25% have about equal probability. No significant correlation is found between T_e/T_i less than one and particular H^+ or He^+ fractions. The distribution of He^+ fractions has a strong peak at about zero with frequency of over 0.6, which is narrower than the proton fraction. The wider He^+ distribution is also seen by the fact that the standard deviation is three times larger than the mean, whereas the H^+ standard deviation is only 1.61 larger than its mean. The median of the He^+ fraction distribution is 0.00000, since half of the spectral fits did not find He^+. The mean He^+/N_e is 0.03 versus 0.13 for H^+/N_e, that is, the radar sees four times more H^+ than He^+. Thus, the two ion fractions have different distributions, consistent with having different production and loss processes.

15. The distribution of radial (line-of-sight) velocities at 589 km is symmetric about zero, with 95% of the velocities within ± 100 m s^{-1}. The median velocity is zero, and the mean is -0.09 m s^{-1}. Therefore, there is no net plasma flow across 589 km on average. Zero velocity is the most frequent value.

16. About 96% of all the data corresponds to Ap values of 27 of less, corresponding to quiet conditions ($Kp \leq 4$). Therefore, only distribution values with cumulative frequencies of less than 4% can be directly attributed to high geomagnetic activity.

5. Acknowledgements.

6. References

Anderson, D. E., and R. R. Meier, The OII 834 Å dayglow: a general model for excitation rate and intensity calculations, *Planet. Space Sci., 33*, 1179, 1985.

Anderson, D. N., M. Mendillo, and B. Herniter, A semi-empirical low-latitude ionospheric model, *Radio Science, 22*, 292, 1987.

Bailey, G. J., and R. Sellek, A mathematical model of the Earth's plasmasphere and its application in a study of He$^+$ at L=3, *AG, 8*, 171, 1990.

Bailey, G. J., J. F. Vickrey, and W. E. Swartz, The topside ionosphere above Arecibo during summer at sunspot minimum and the influence of an interhemispheric flow of thermal protons, *JGR, 87*, 7557, 1982.

Bauer, S. J., Chemical processes involving helium ions and the behavior of atomic nitrogen ions in the upper atmosphere, *JGR, 71*, 1508, 1966.

Behnke, R. A., and R. M. Harper, Vector measurements of F region ion transport at Arecibo, *JGR, 78*, 8222, 1973.

Breig, E. L., S. Sanatani, and W. B. Hanson, Thermospheric hydrogen: The long-term solar influence, *J. Geophys. Res., 90*, 5247, 1985.

Burnside, R. G., C. A. Tepley, and M. P. Sulzer, World day observations at Arecibo: 1985 to 1989, *J. Geophys. Res., 96*, 3691, 1991.

Burnside, R. G., J. C. G. Walker, and M. P. Sulzer, Kinematic properties of the F-region ion velocity field inferred from incoherent scatter radar measurements at Arecibo, *JGR, 92*, 3345, 1987.

Carlson, H. C., Ionospheric heating by magnetic conjugate-point photoelectrons, *JGR, 71*, 195, 1966.

Carlson, H. C., and W. E. Gordon, Radar spectrographic estimates of ionic composition from 225 to 1400 kilometers for solar minimum winter and summer conditions, *JGR, 71*, 5573, 1966.

Carpenter, L. A., and S. A. Bowhill, Investigation of the physics of dynamical processes in the topside F region, Aeronomy Report No. 44, University of Illinois, Urbana, Illinois, 1971.

Chapman, S., The absorption and dissociative or ionizing effect of monochromatic radiation in an atmosphere on a rotating earth, *Proc. Phys. Soc., 43*, 484, 1931.

Erickson, P. J., and W. E. Swartz, Mid-latitude incoherent scatter observations of helium and hydrogen ions, *GRL, 21*, 2745, 1994.

Evans, J. V., Theory and practice of ionosphere study by Thomson scatter radar., *Proc. IEEE, 57*, 495, 1969.

Evans, J. V., and M. Loewenthal, ionospheric backscatter observations, *PSS, 12*, 915, 1964.

Farley, D. T., Radio wave scattering from the ionosphere, in *Methods of Experimental Physics, 92*, 139, Academic Press, New York and London, 1971.

Fejer, B. G., F region plasma drifts over Arecibo: Solar cycle, seasonal, and magnetic activity effects, *JGR, 98*, 13645, 1993.

Fox, M. W., A simple, convenient formalism for electron density profiles, *Radio Sci., 29*, 1473, 1994.

Ganguly, S., R. A. Behnke, and B. A. Emery, Average electric field behavior in the ionosphere over Arecibo, *JGR, 92*, 1199, 1987.

González, S. A., B. G. Fejer, R. A. Heelis, and W. B. Hanson, Ion composition of the topside equatorial ionosphere during solar minimum, *J. Geophys. Res., 97*, 4299, 1992.

González, S. A., and M. P. Sulzer, Detection of He$^+$ layering in the topsider ionosphere over Arecibo during equinox solar minimum, *Geophys. Res. Letters, 23*, 2509, 1996.

Grebowski, J. M., W. R. Hoegy, and T. C. Chen, High latitude field aligned light ion flows in the topside ionosphere deduced from ion composition and plasma temperatures, *JATP, 55*, 1605, 1993.

Hagen, J. B., and P. Y. Hsu, The structure of the protonosphere above Arecibo, *J. Geophys. Res., 79*, 4269, 1974.

Harper, R. M., Nighttime meridional neutral winds near 350 km at low to mid-latitudes, *JATP, 35*, 2023, 1973.

Hedin, A. E., MSIS-86 thermospheric model, *J. Geophys. Res., 92*, 4649, 1987.

Ho, M. C., and D. R. Moorcroft, Hydrogen density and proton flux in the topside ionosphere over Arecibo, Puerto Rico, from incoherent scatter radar observations, *PSS, 19*, 1441, 1971.

Hoegy, W. R., J. M. Grebowski, and L. H. Brace, Ionospheric ion composition from satellite measurements made during 1970-1980: Altitude profiles, *Adv. Space Res., 11(10)*, 10(173), 1991.

Kelley, M. C. and R. A. Heelis, *The Earth's Ionosphere, Plasma Physics and Electrodynamics*, Academic Press, San Diego, 1989.

Köhnlein, W., Electron temperature variations during solar maximum conditions (200-3500 km), *PSS, 29*, 47, 1981.

Kutiev, I., R. A. Heelis, and S. Sanatani, The behavior of the O^+--H^+ transition level at solar maximum, *JGR, 85*, 2366, 1980.

Mahajan, K. K., 10.7 cm-Solar radio flux and ionospheric temperatures, *JATP, 29,* 115, 1967.

Mathews, J. D., Incoherent scatter radar probing of the 60-100-km atmosphere and ionosphere, *IEEE Trans. Geoscience and Remote Sensing, GE-24,5,* 765, 1986.

Menke, W., *Geophysical Data Analysis: Discrete Inverse Theory, Intl. Geophys. Ser., No. 45*, Academic, San Diego, 1989.

Moorcroft, D. R., Nighttime topside ionic composition and temperature over Arecibo, Puerto Rico, *JGR, 74*, 315, 1969.

Picone, J. M., R. R. Meier, K. F. Dymond, R. P. McCoy, O. Kelley, and R. J. Thomas, Calculation of the O^+ concentration from O II 834 Å airglow using discrete inverse theory, NRL Memorandum Report 7643—95—7772, Naval Research Laboratory, 1995.

Picone, J. M., R. R. Meier, O. A. Kelley, D. J. Meléndez-Alvira, K. F. Dymond, and R. P. McCoy, Discrete inverse theory for 834- Å ionospheric remote sensing, *Radio Sci., 32,* 1973-1984, 1997.

Prasad, S. S., Nighttime ionic composition and temperature over Arecibo, *JGR, 73,* 6795, 1968.

Press, W. H., B. P. Flannery, S. A. Teukolsky, and W. T. Vetterling, *Numerical Recipes: The Art of Scientific Computing*, Cambridge University Press, New York, 1989.

Rishbeth, H., and O. K. Garriott, *Introduction to Ionospheric Physics, Int. Geophys. Ser.*, vol. 14, Academic Press, San Diego, Calif., 1969.

Roble, R. G., The calculated and observed diurnal variation of the ionosphere over Millstone Hill on March 23-24, 1970, *PSS, 23*, 1017, 1975.

Rodgers, C. D., Retrieval of atmospheric temperature and composition from remote measurements of thermal radiation, *Rev. Geophys. and Space Phys., 14*, 609, 1976.

Schunk. R. W., and A. F. Nagy, Electron temperatures in the F region of the ionosphere: Theory and observations, *RGSP, 16*, 355, 1978.

Schunk. R. W., and J. C. G. Walker, Minor ion diffusion in the F2-region of the ionosphere, *PSS, 18*, 1319, 1970.

Strickland, D. J. and T. M. Donahue, Excitation and radiative transport of OI 1304 Å resonance radiation – I. The dayglow, *Planet. Space Sci., 18*, 661, 1970.

Sulzer, M. P., A radar technique for high range resolution incoherent scatter autocorrelation function measurements utilizing the full average power of klystron radars, *RS, 21,* 1033, 1986.

Sulzer, M. P., and S. A. González, Simultaneous measurements of O^+ and H^+ temperatures in the topside ionosphere over Arecibo, *GRL, 23,* 3235, 1996.

Suvanto, K., On the analysis of incoherent scatter radar data from non-thermal ionospheric plasma: Effects of measurement noise and an inexact theory, *Planet. Space Sci., 38,* 903, 1990.

Swartz, W. E., and J. S. Nisbet, Incompatibility of solar EUV fluxes and incoherent scatter measurements at Arecibo, *JGR, 78,* 5640, 1973.

Tarantola, A., and B. Valette, Generalized nonlinear inverse problems solved using the least squares criterion, *Rev. Geophys. Space Phys., 20,* 219, 1982.

Tarantola, A., *Inverse Problem Theory: Methods for Data Fitting and Model Parameter Estimation*, chapter 4, Elsevier, New York, 1987.

Tepley, C. A., and R. B. Kerr, Variations in the proton concentration and flux of the topside ionosphere at Arecibo during the September 1984 equinox transition study, *JGR, 94,* 16977, 1986.

Tepley, C. A., and R. B. Kerr, Temporal, seasonal and solar cycle variations of the topside proton concentration over Arecibo, *Adv. Space Res., 7(10)*, 291, 1987.

Tinsley, B. A., Effects of charge exchange involving H and H^+ in the upper atmosphere, *PSS, 26*, 847, 1978.

Figures

1. Distribution of daily 10.7-cm solar flux (F10.7) values corresponding to the dataset of ten years of Arecibo World days between 1985 and 1995. About 55% of the distribution has F10.7 greater than 120.

2. Distribution of years covered in the dataset beginning late in 1985 and extending to 1995.

3. Distribution of months covered in the Arecibo World day database between 1985 and 1995. January is month number one.

4. Distribution of local times corresponding to the fits to ten years of Arecibo World days between 1985 and 1995. Midnight is 0. Nearly all local times were sampled equally.

5. Virtually all ten years of World day observations were made with the antenna beam pointed at an elevation angle of 75° (zenith angle of 15°) while the azimuth angle was changed.

6. Two distributions of F_2 peak densities are shown: the linear-H fits (solid line, "nmax") to the measured electron density profiles contained in the database, and splines fits (broken line, "Nmax"). The horizontal scale is in electrons per 10^6 cm^{-3} (10^{12} m^{-3}). The CEDAR database Nmax are obtained with cubic splines.

7. Two distributions of F_2 peak heights are shown: the linear-H fits (solid line, "hmax") to the measured electron density profiles contained in the CEDAR database, and the splines fits (dotted line, "zmax"). The horizontal scale is the peak height in km. Splines do not account for random experimental noise.

8. Distribution of the $\log_{10}$(reduced χ^2) values obtained in fitting 9801 electron density profiles. The distribution is centered at 0 ($\chi^2 = 1$).

9. Distribution of the percentage model uncertainty in the linear-H F_2 peak density (nmax).

10. Distribution of the percentage uncertainty in the model F_2 layer height (hmax).

11. Distribution of the difference between the linear-H and CEDAR database peak densities, normalized by Nmax (CEDAR database, splines), expressed in percent.

12. Distribution of the difference between the linear-H and CEDAR database peak heights, normalized by zmax (CEDAR database, splines), expressed in percent.

13. Distribution of B, the absolute magnitude of the average residual between the linear-H and measured electron densities for each of the 9801 fitted profiles, normalized by the measured electron densities (Equation 4), expressed as percent. This parameter is a measure of the accuracy and bias of the linear-H fit to the measured profile.

14. Distribution of D, the average of the measurement uncertainties in each electron density profile, normalized by the data, and expressed as percent (Equation 5). This is a measure of the range of data errors, closely resembling the distribution of Fig. 13.

15. The distribution of $B - D$, the difference between the average model and measured residuals for each profile (Fig. 13) and the average measurement error in a profile (Fig. 14). Negative values indicate that experimental errors dominate.

16. Distribution of F, the median of, the absolute magnitude of the residual between the linear-H and measured electron density profiles, normalized by the measurement, and expressed as percent (Equation 6). This is a measure of the median fit residual, which is less sensitive to outliers.

17. Distribution of C, the minima in the ratio of the experimental uncertainty to the linear-H electron density for each profile (Equation 7). This is a measure of the smallest experimental uncertainty as a percentage of the linear-H density.

18. Distribution of the linear-H parameter H_0 (km), a pseudo-scale height term, which controls the shape of the model electron density profile (Equation 1). This parameter takes on values resembling the atomic oxygen scale height.

19. Distribution of the linear-H model parameter, $\log_{10} H_1$, which modifies H_0 and thus the shape of the linear-H electron density profile above hmax (Equation 1). The parameter H_1 is the linear gradient in the pseudo-scale height, which assumes a particular value for each model profile.

20. Distribution of the percentage error in H_0 (the linear-H uncertainty divided by H_0).

21. Distribution of the percentage error in H_1 (the linear-H uncertainty divided by H_1).

22. Distribution of the electron temperature measured at 589 km as recorded in the dataset of ten years of Arecibo World days. The horizontal scale is degrees K. The T_e distribution is bimodal, a feature consistent with solar cycle and diurnal control.

23. Distribution of the ratio of electron to ion temperatures, T_e/T_i, measured at 589 km. Values of T_e/T_i less than one comprise are an artifact of the radar spectral fits. Only 13% of the ratios are smaller than one.

24. Distribution of electron densities measured at 589 km. The horizontal scale is in units of electrons per 10^{12} m^{-3} (10^6 cm^{-3}).

25. Distribution of proton fractions (H^+/Ne) measured at 589 km.

26. Distribution of Helium ion fractions (He^+/Ne) measured at 589 km.

27. Distribution of radial (line-of-sight) ion velocities along the antenna beam as measured at 589 km (see equation 7). The distribution is centered at zero velocity, indicating no net up or down ion motion. Positive velocities are up along the beam

28. Distribution of Ap, the global average of the 3-hourly ap values. Ap values of 27 correspond to Kp = 4; Ap = 48 corresponds to Kp = 5, which denotes magnetically disturbed conditions. About 4% of the World day profiles correspond to Ap values indicating disturbed conditions.

29. Composite panel of all the figures previously shown.

Figure-- 1

DMA\pcuap6\\f:\rdpavr\arecibo_code\PLOT_ARECIBO_OK_T.PRO\\(ONE_HISTOGRAM)\\16-Nov-1998 15:53
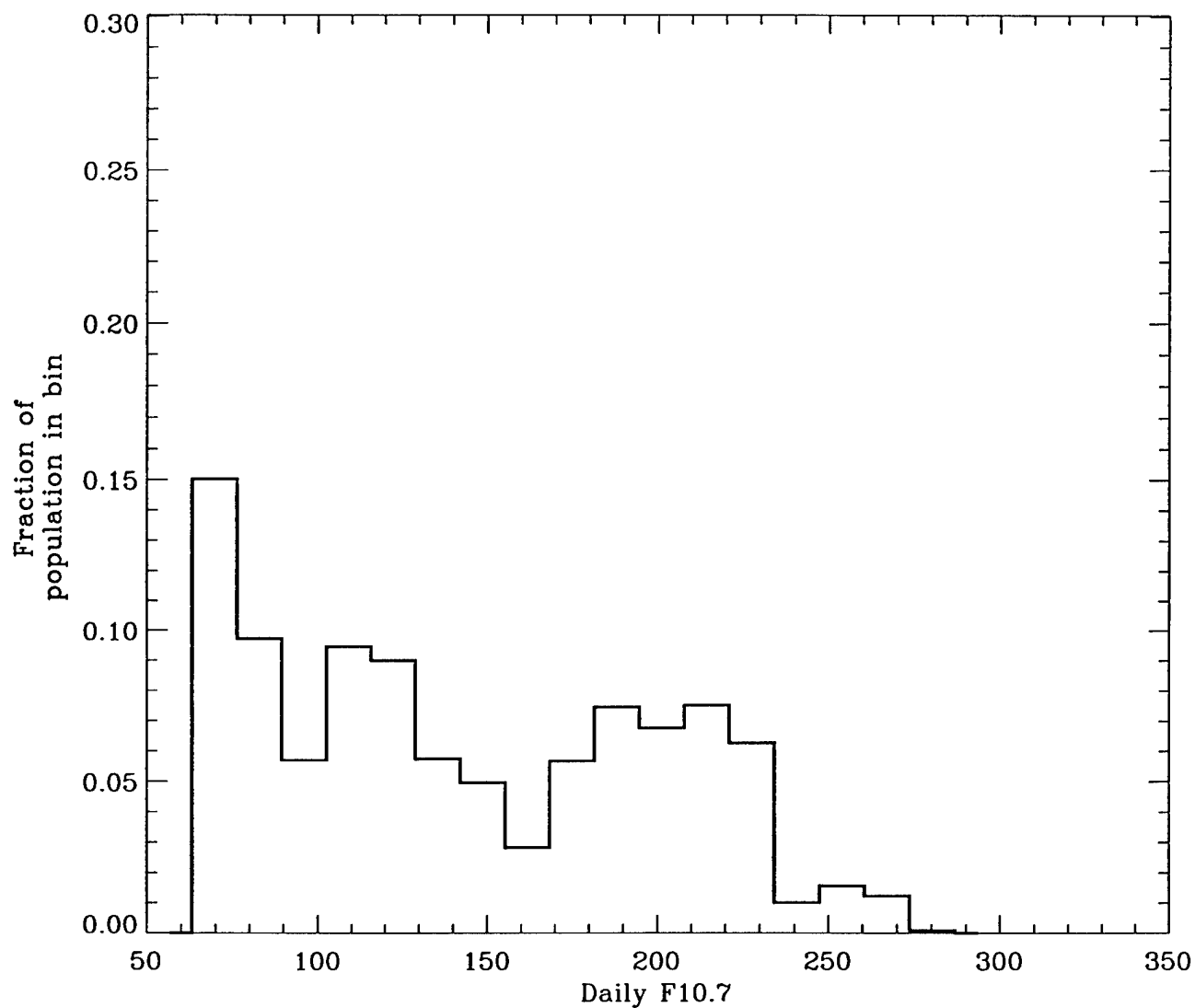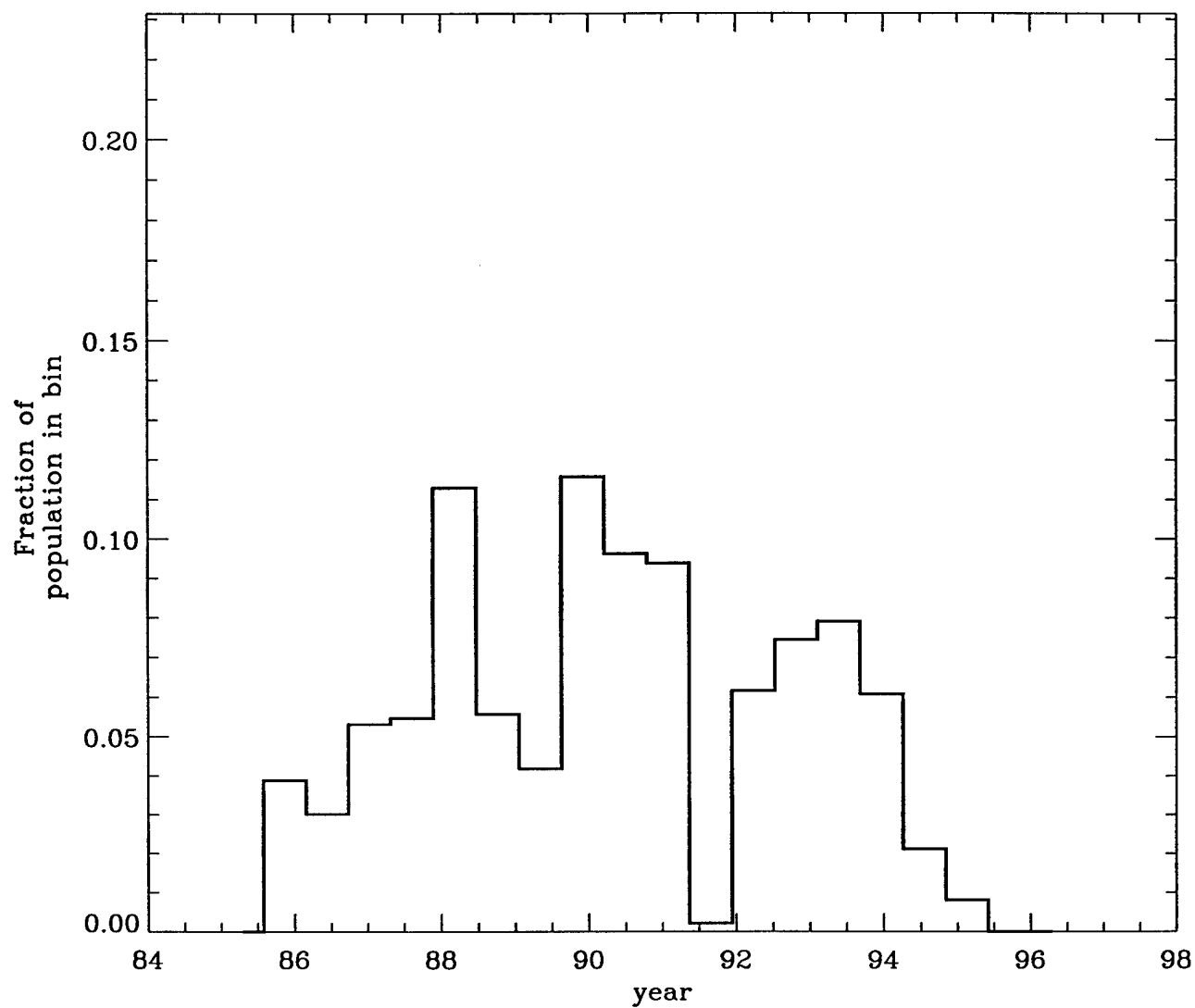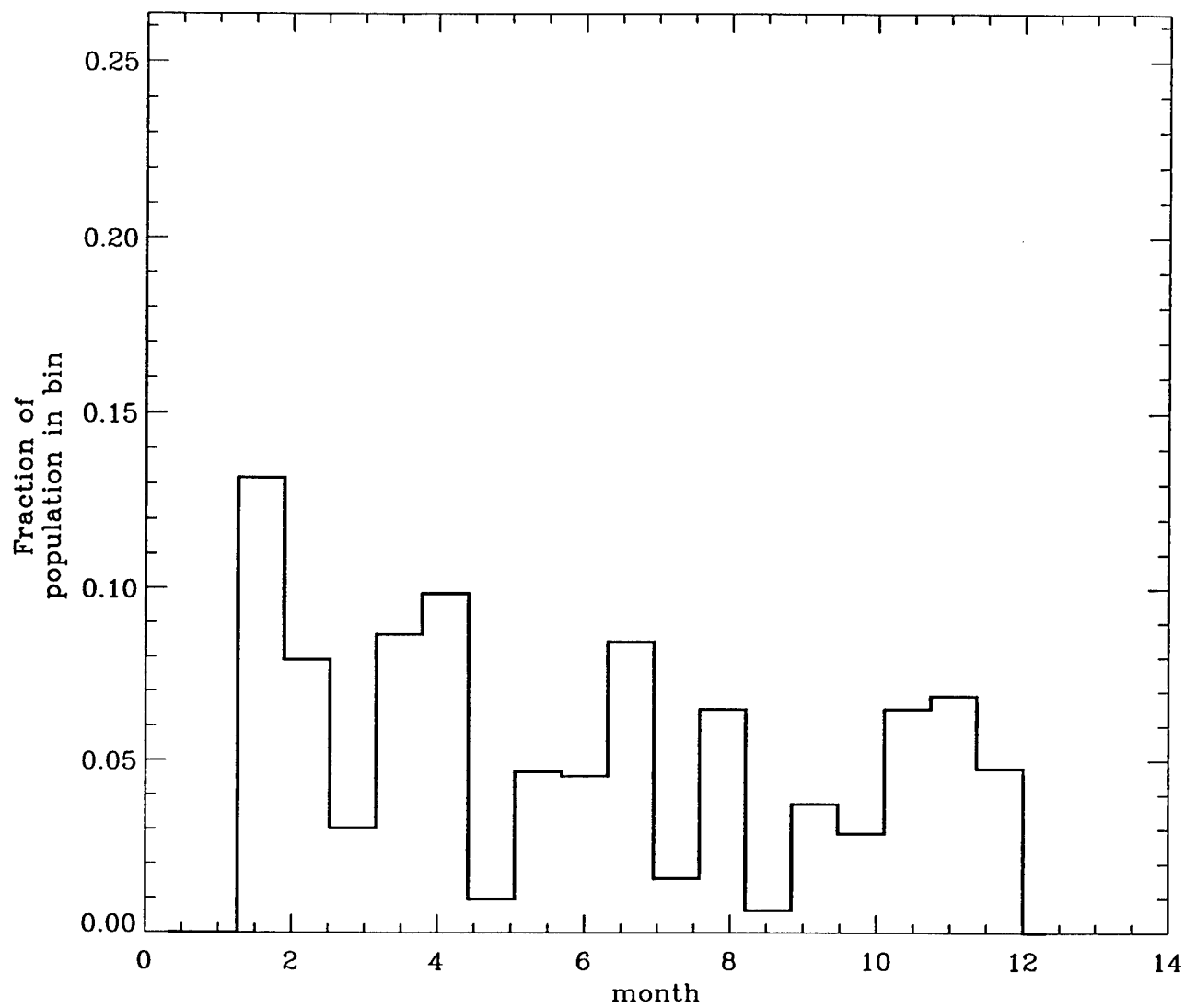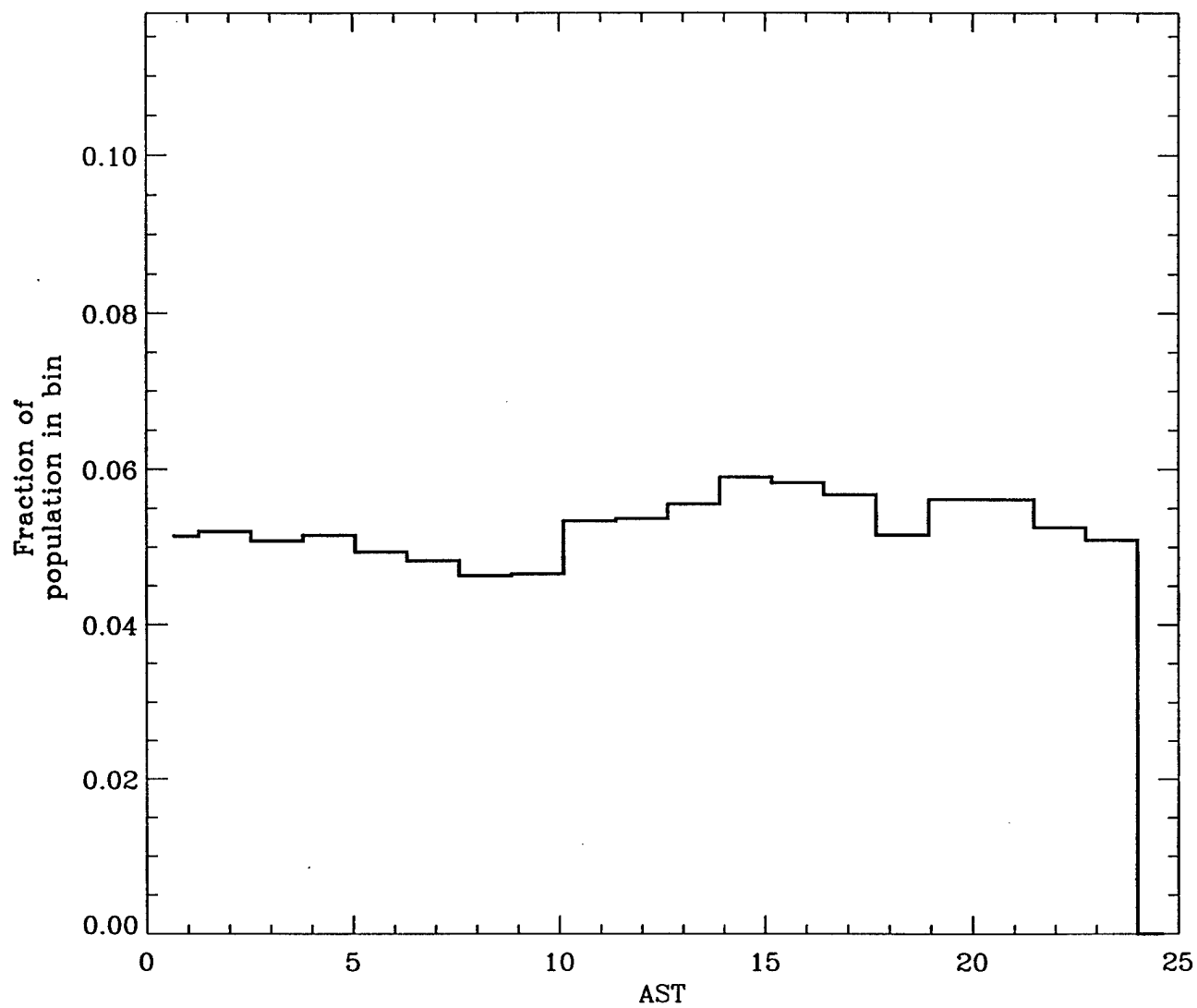
Figure-- 2

Figure-- 3

Figure-- 4
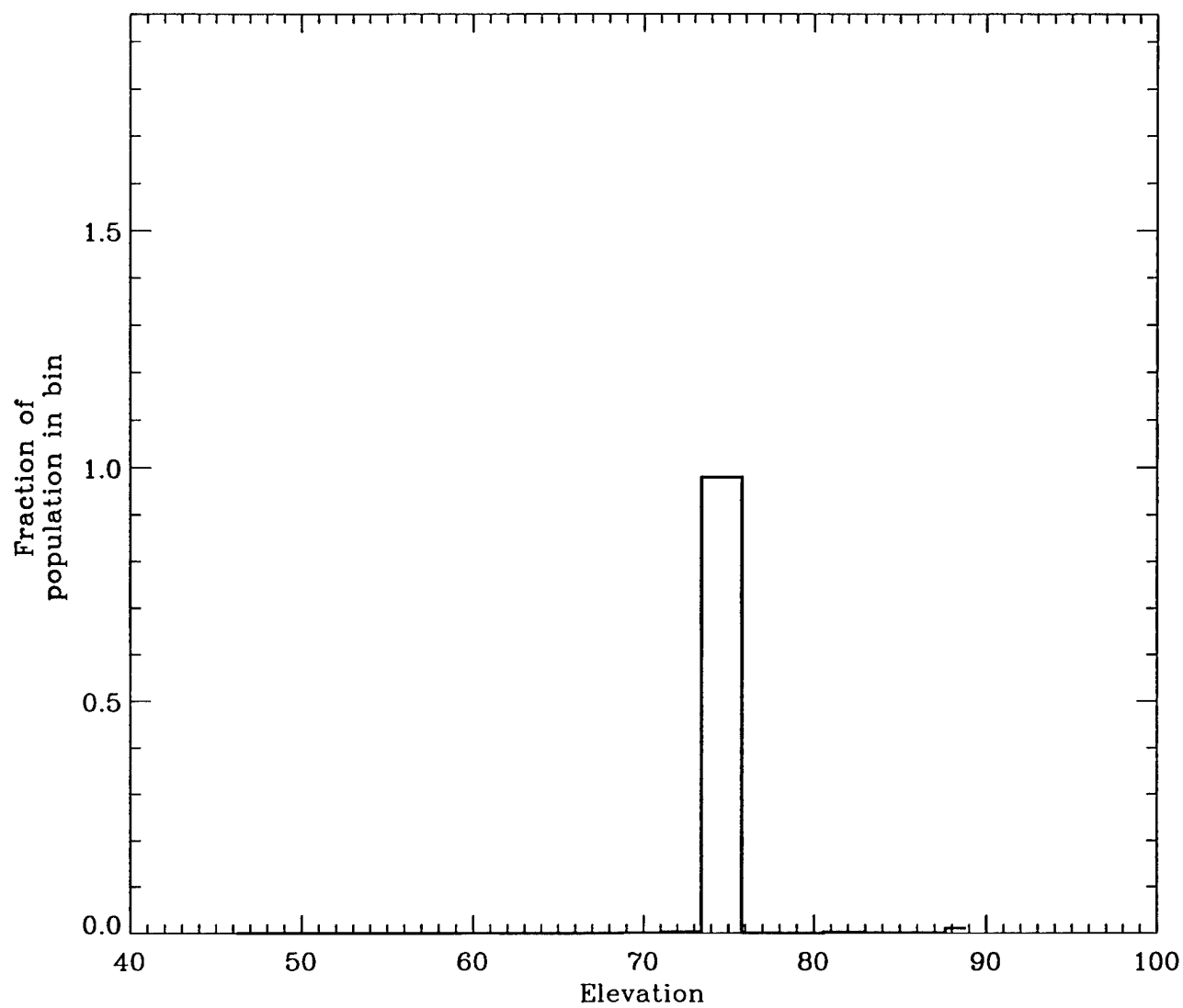
Figure-- 5
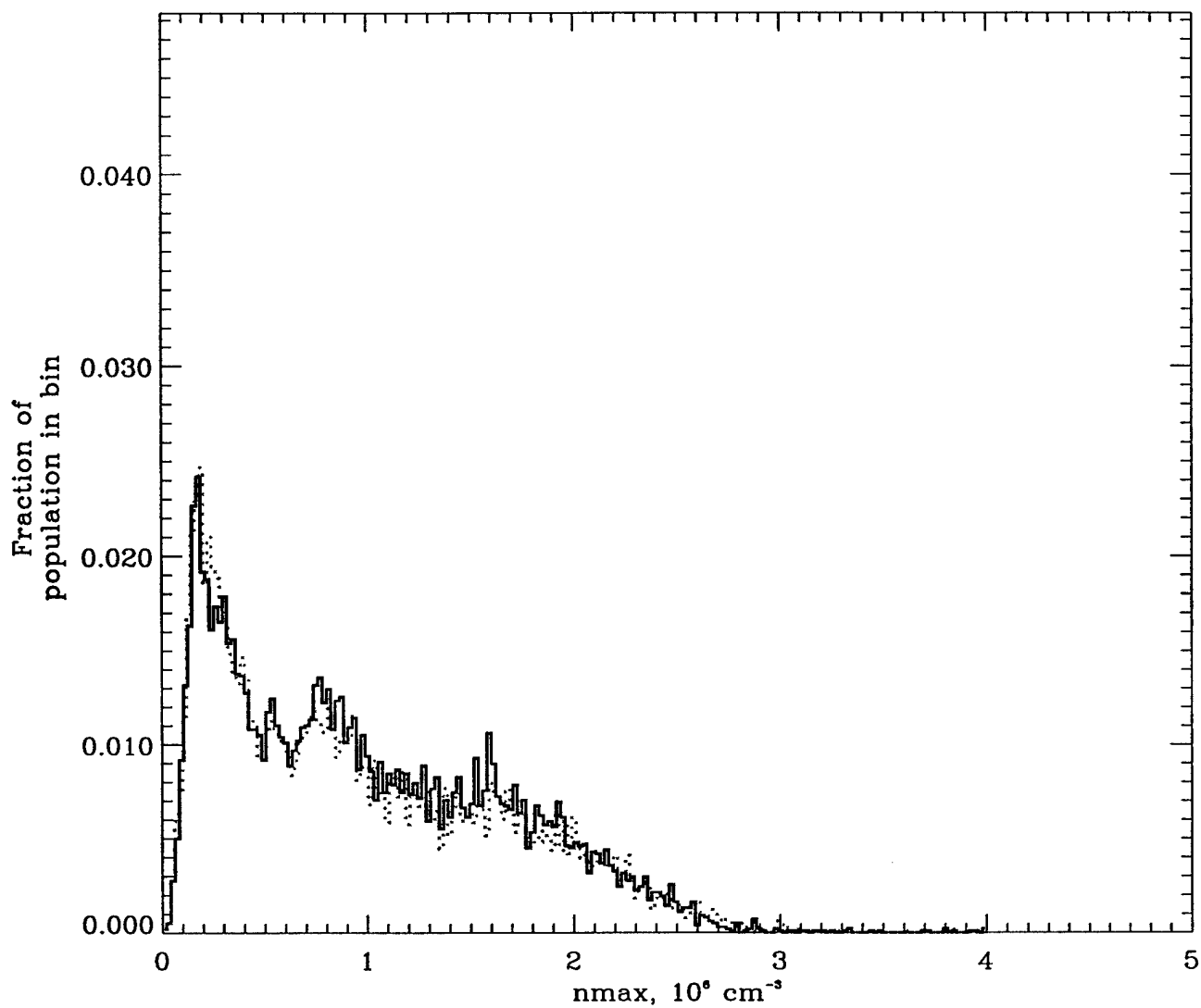
Figure-- 6
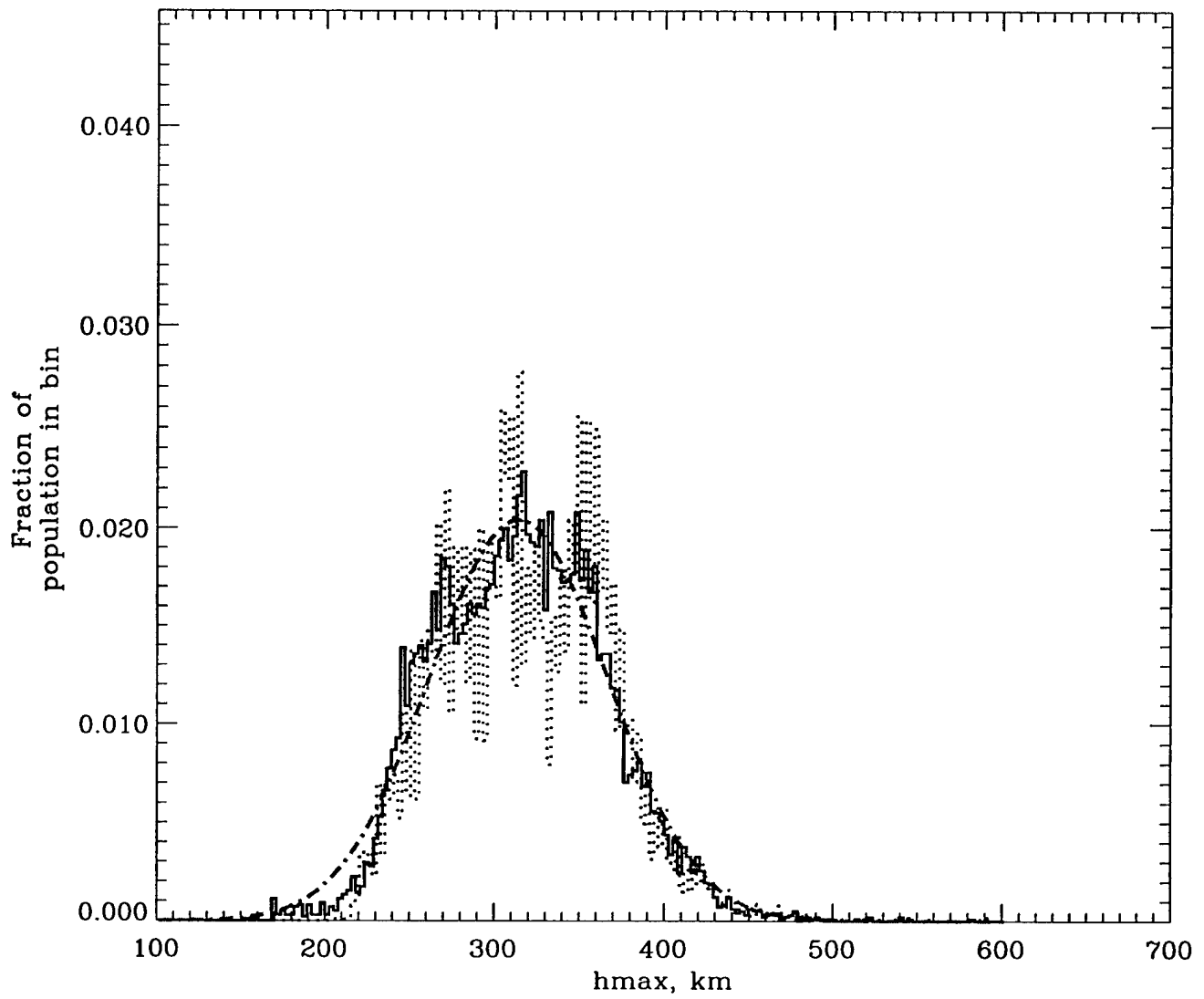
Figure-- 7
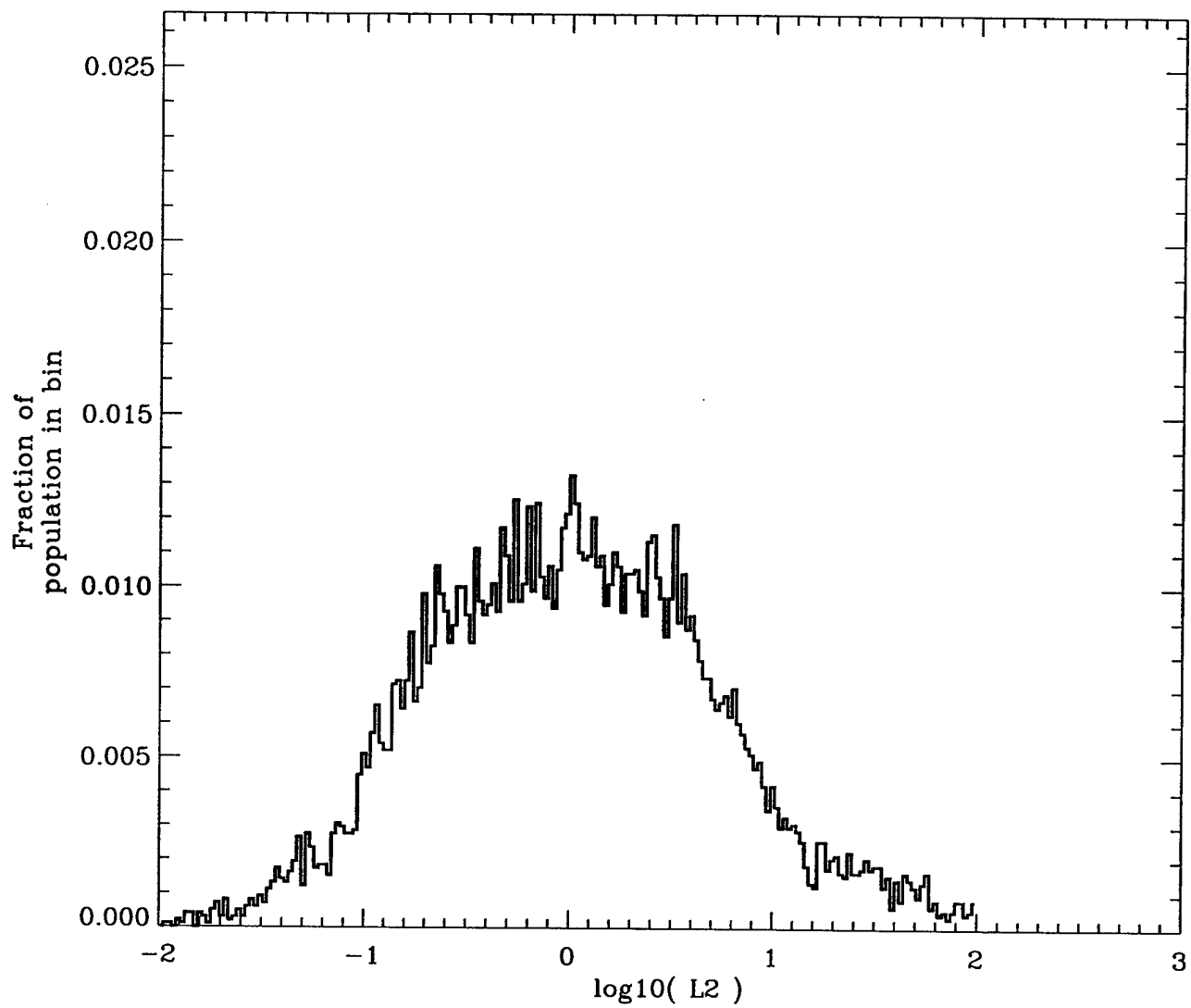
Figure-- 8
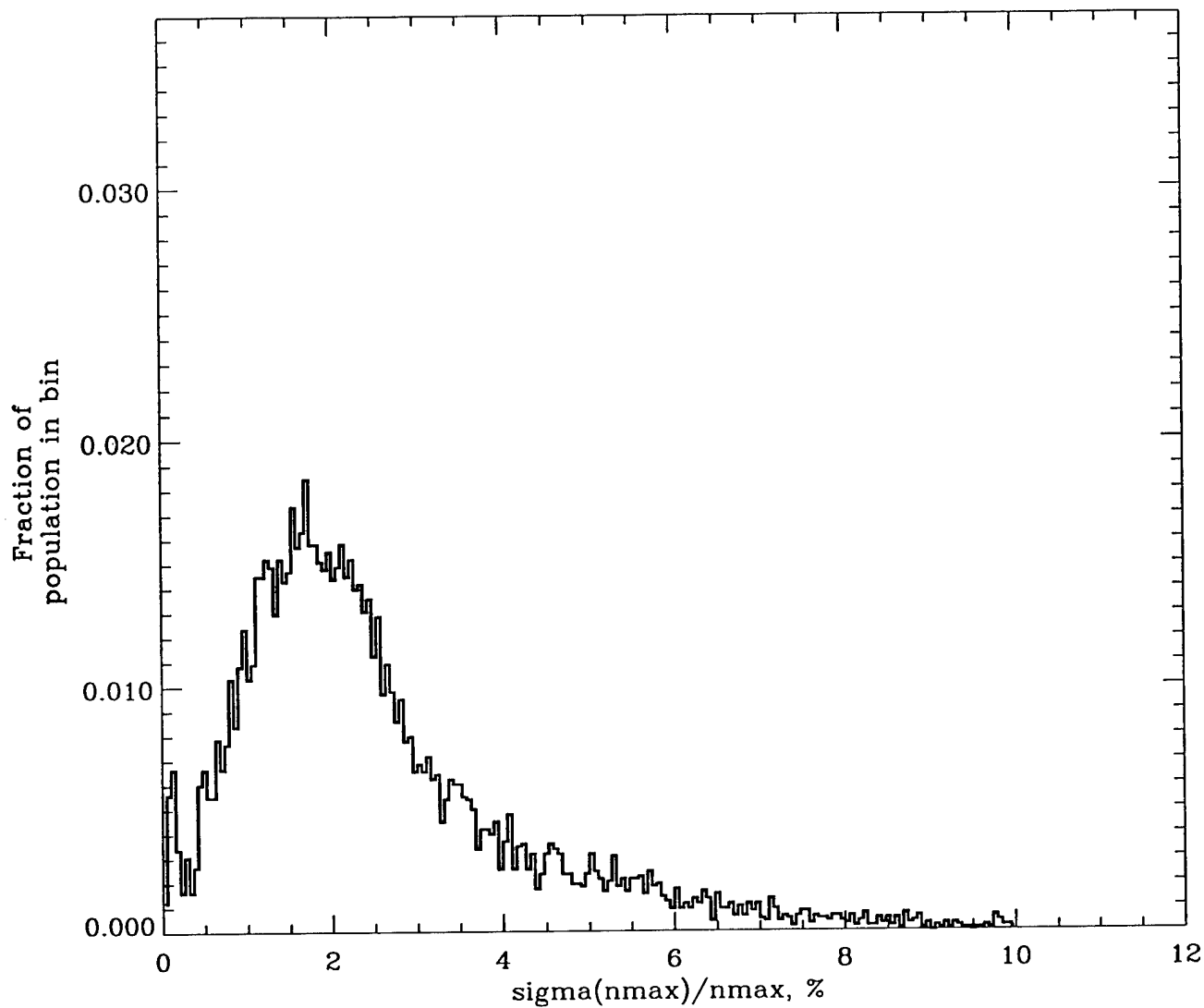
Figure-- 9
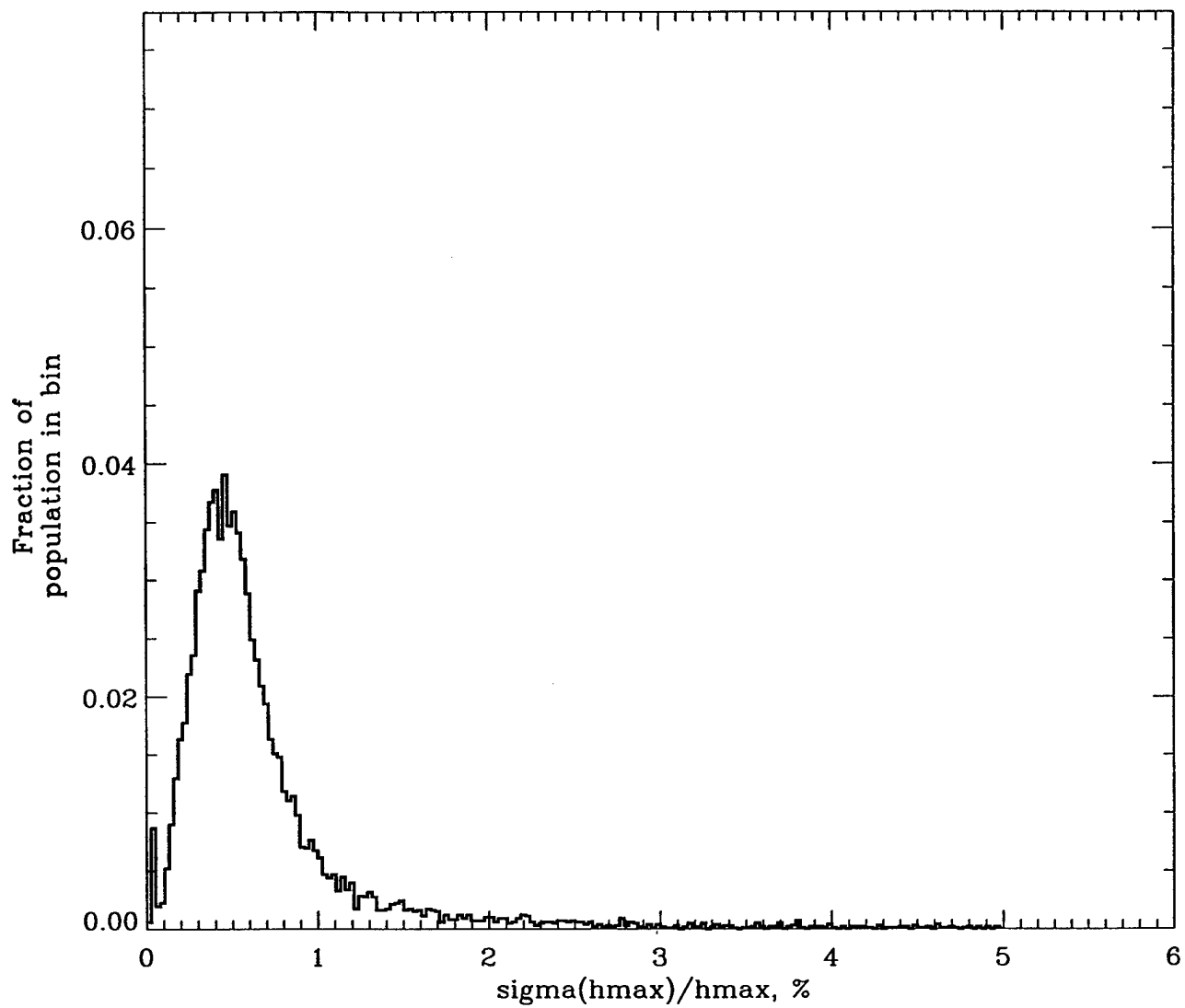
Figure-- 10
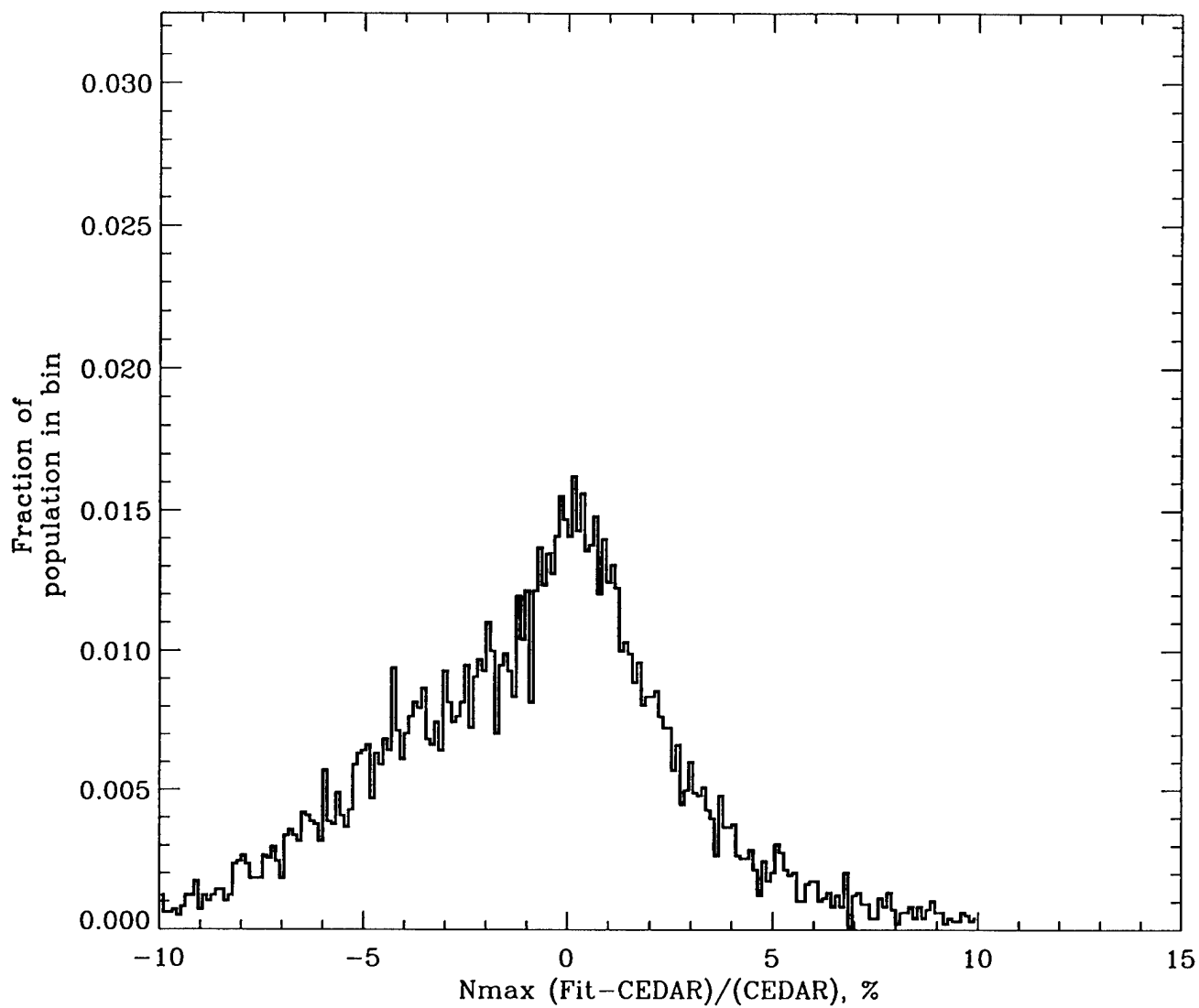
Figure-- 11
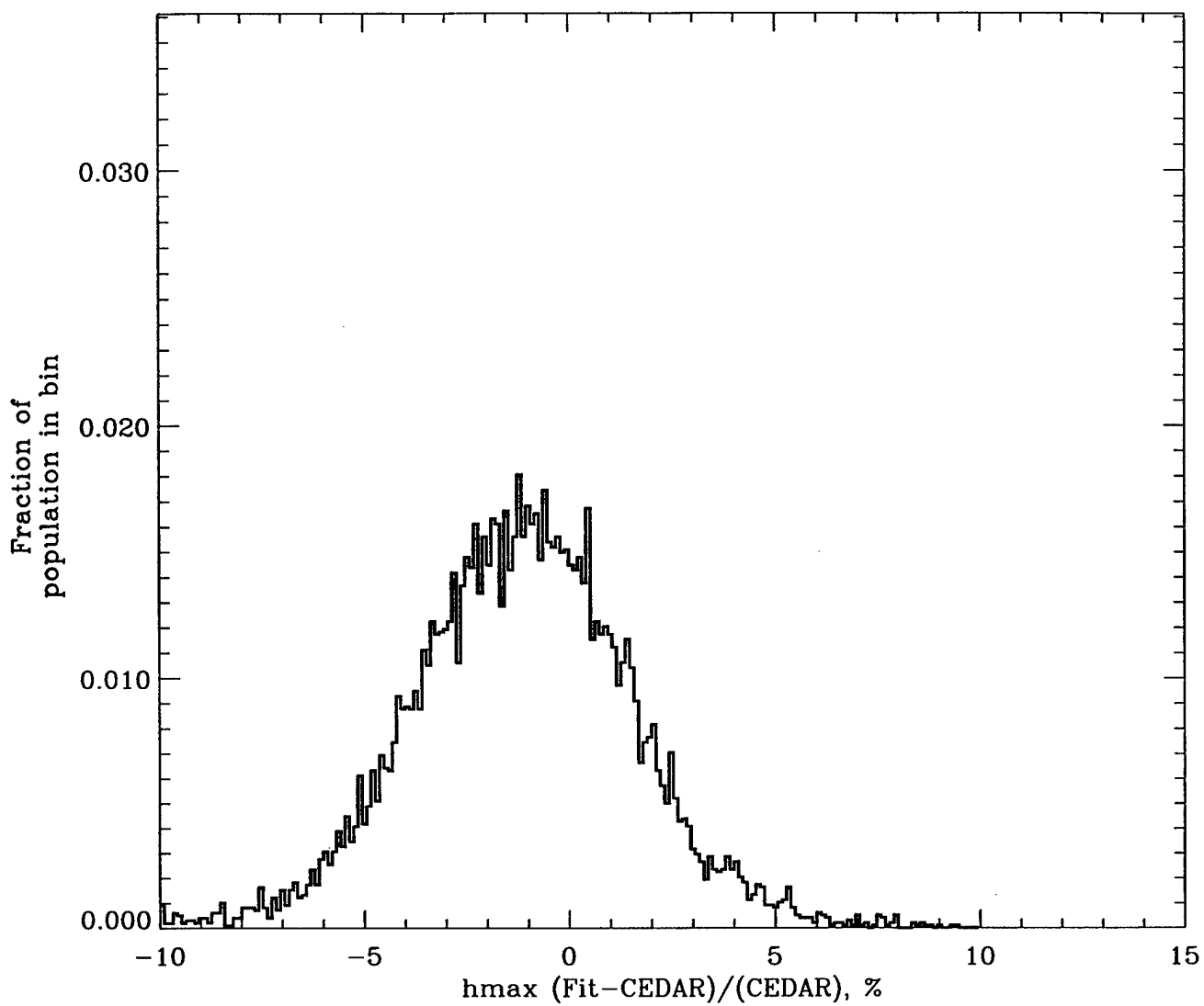
Figure-- 12
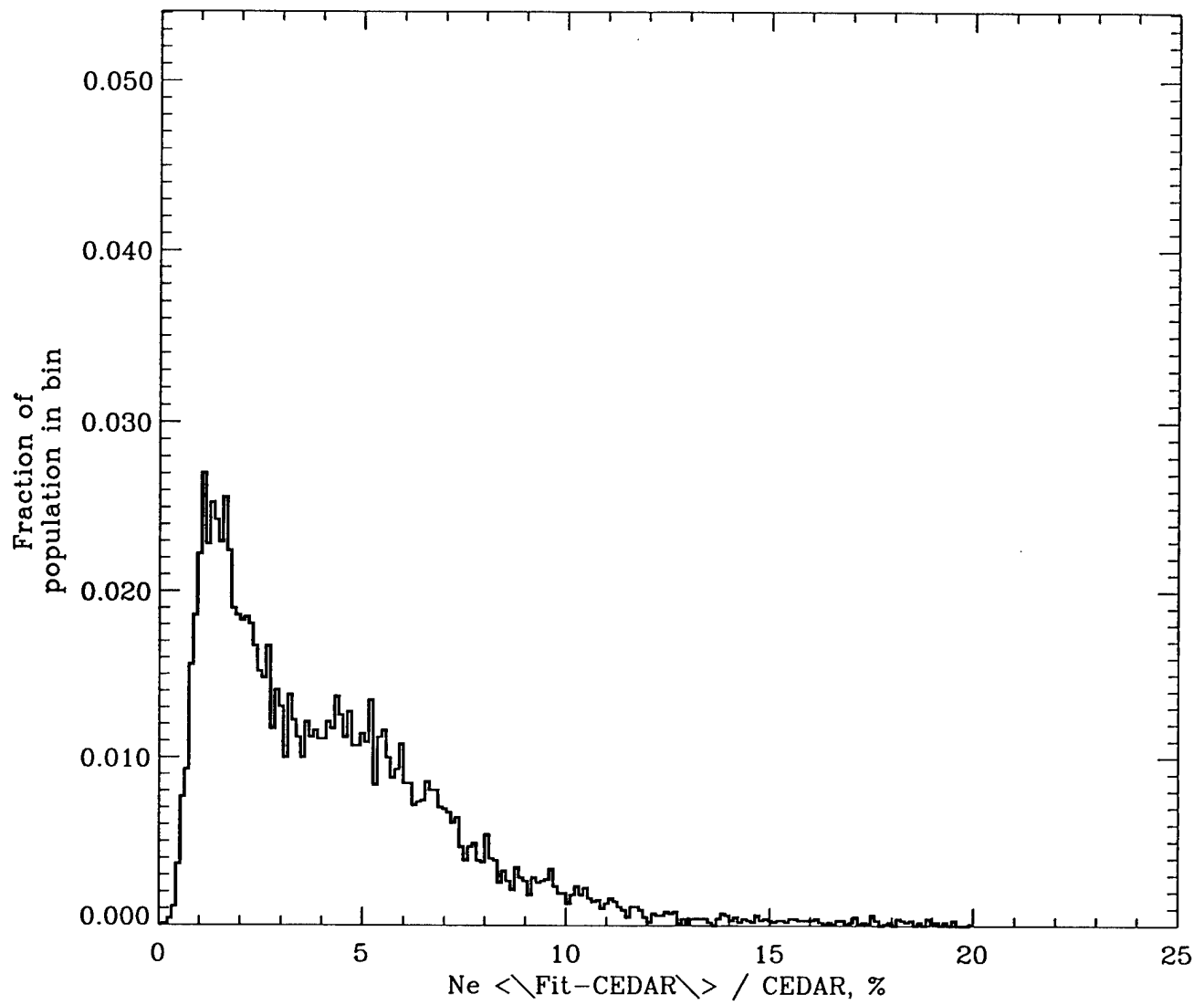
Figure-- 13
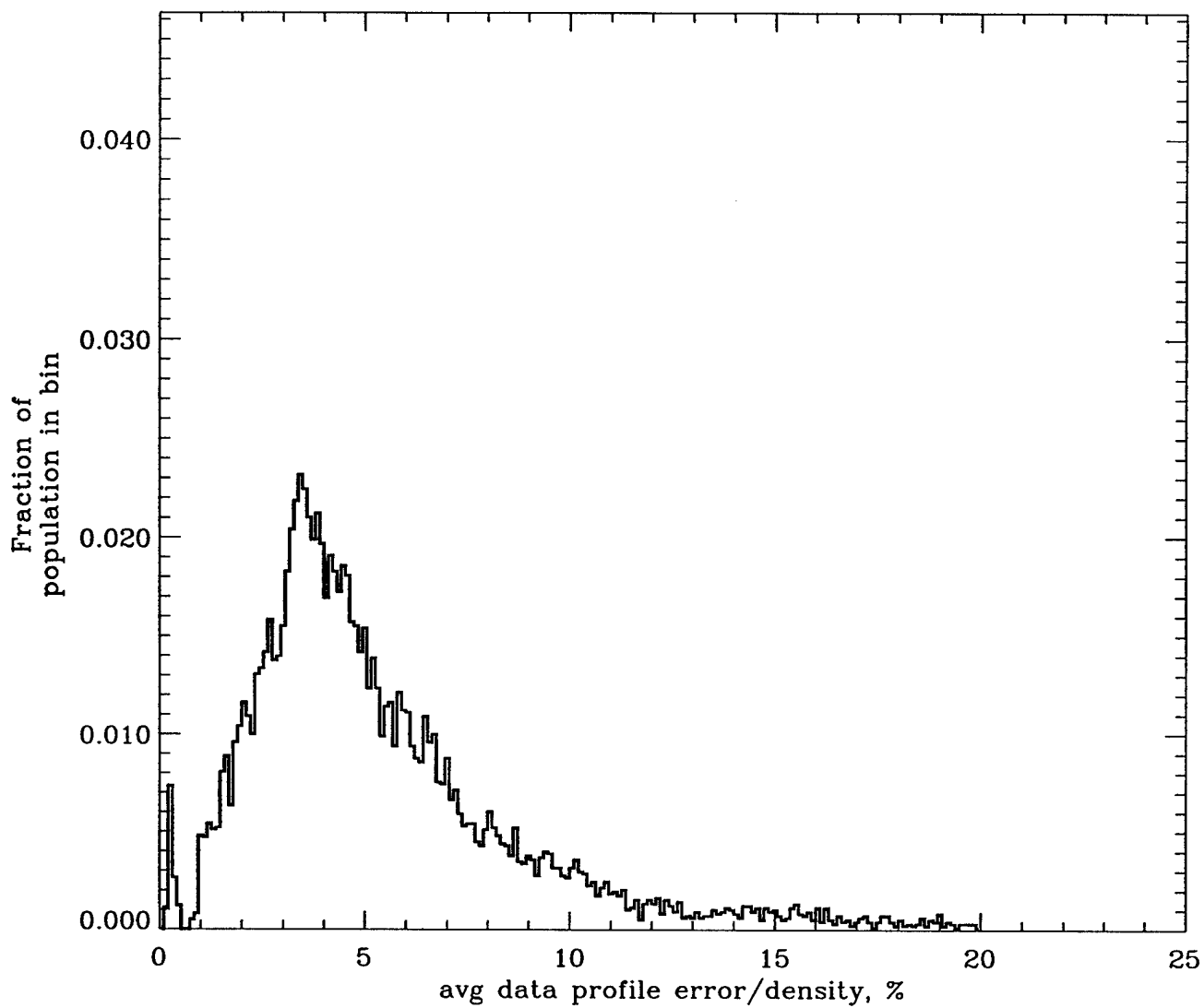
Figure-- 14
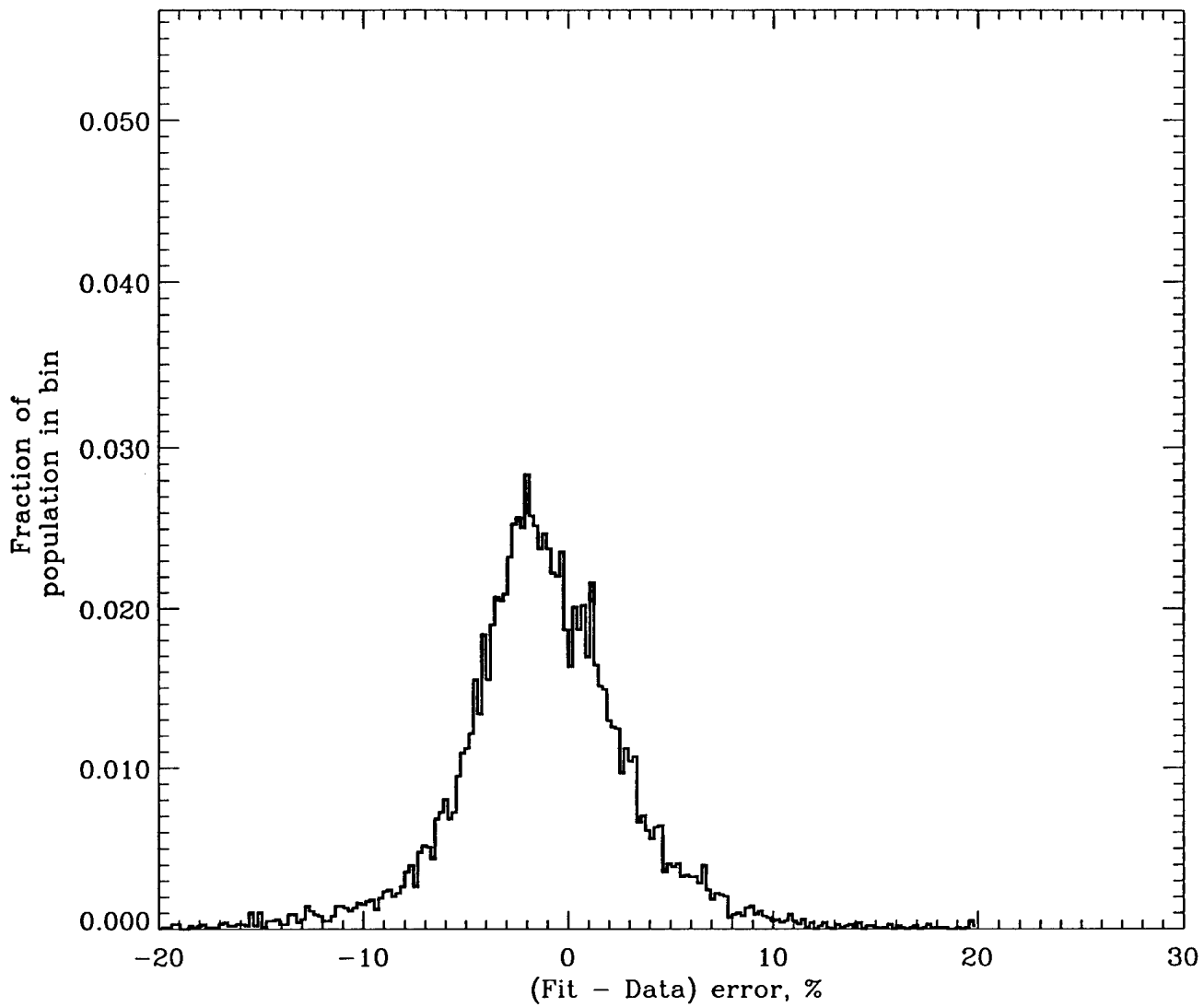
Figure-- 15
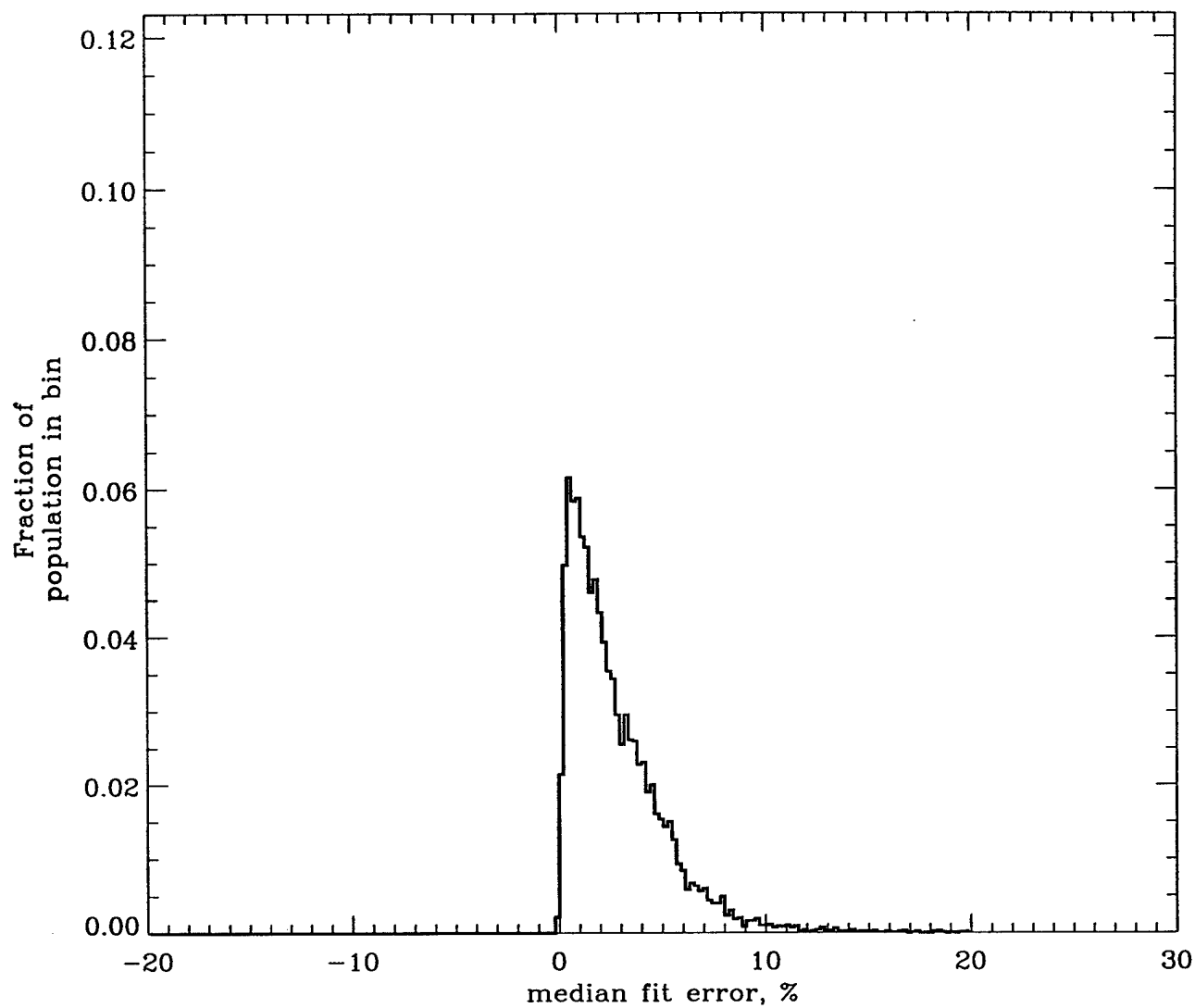
Figure-- 16
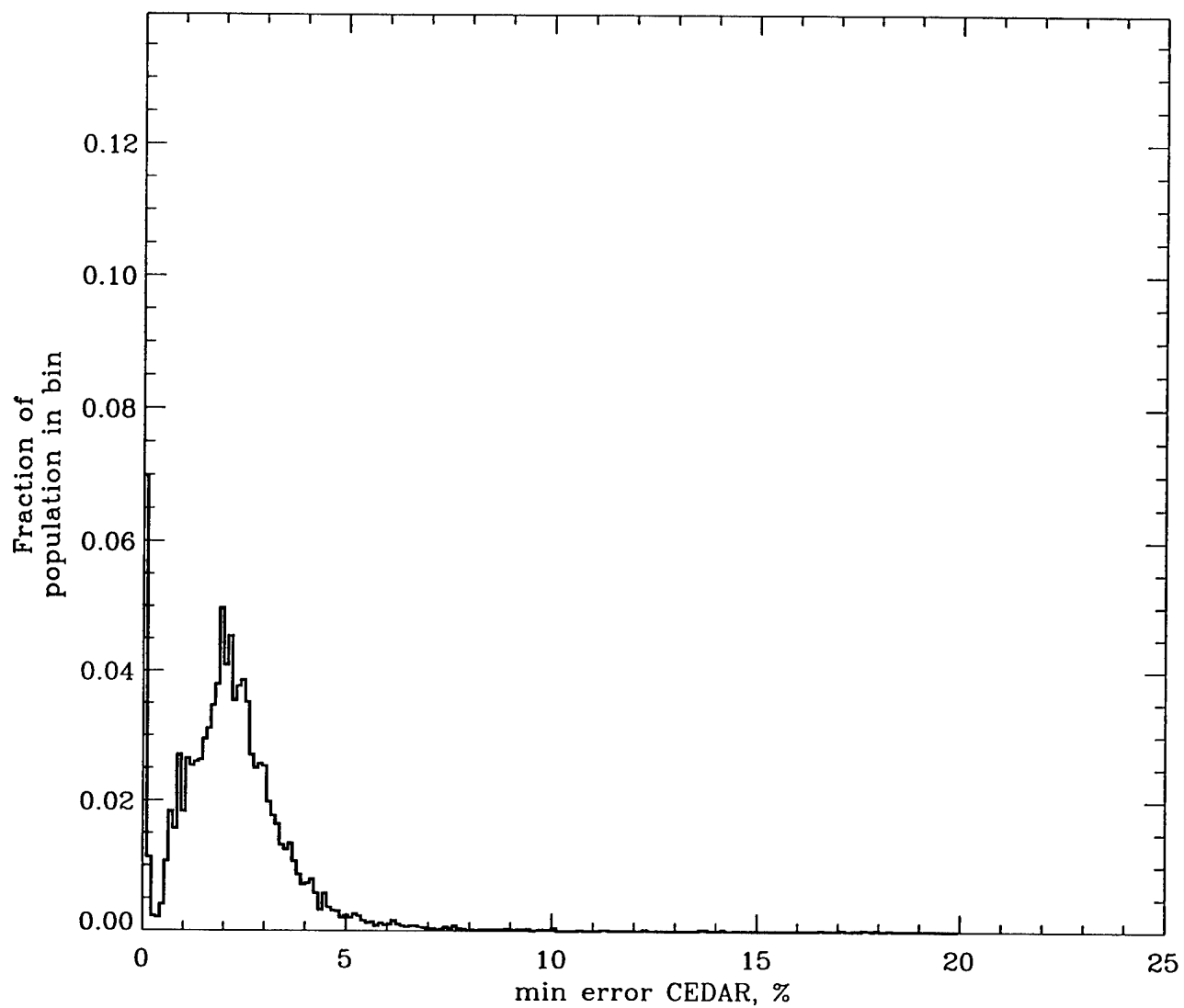
Figure-- 17
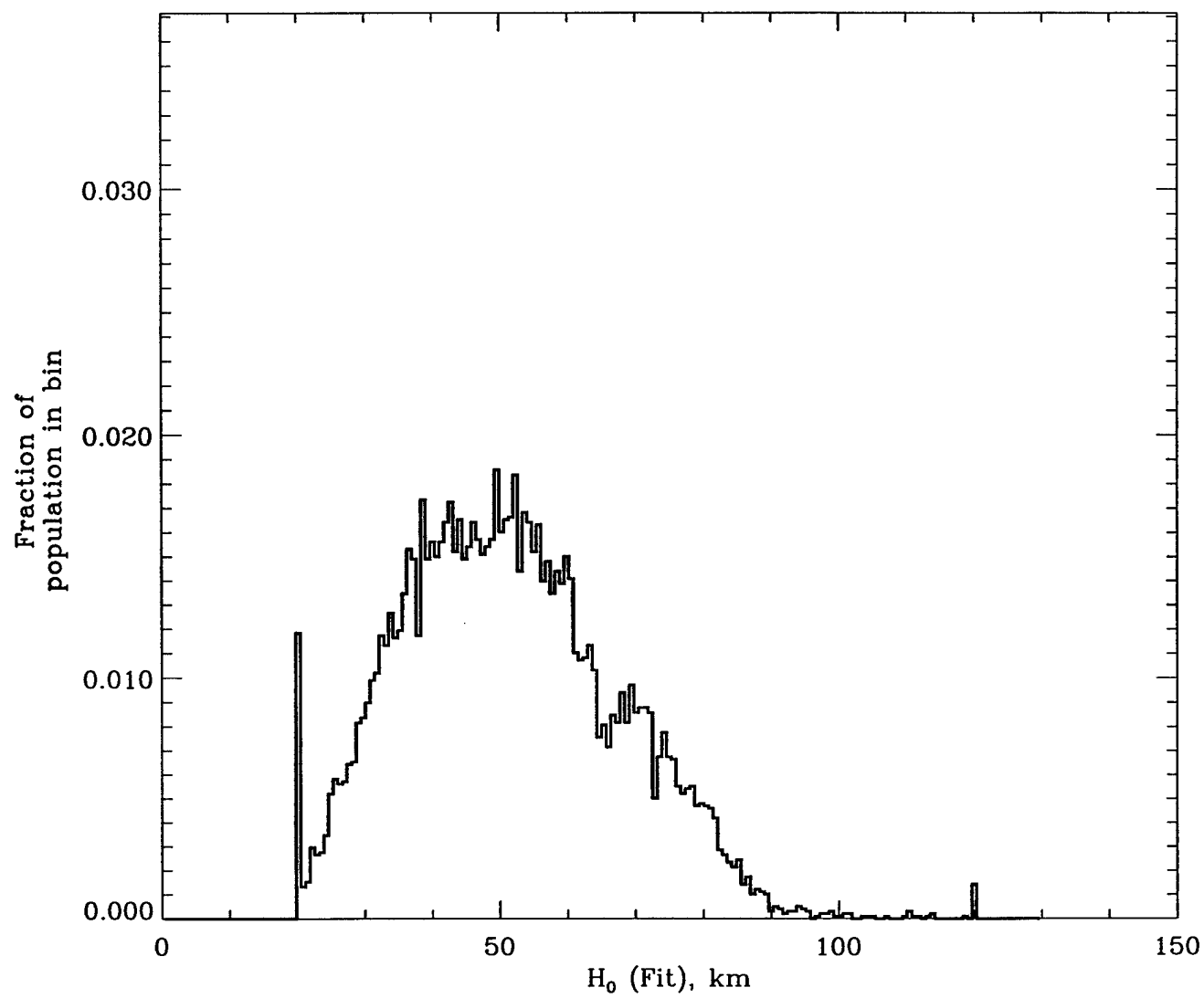
Figure-- 18
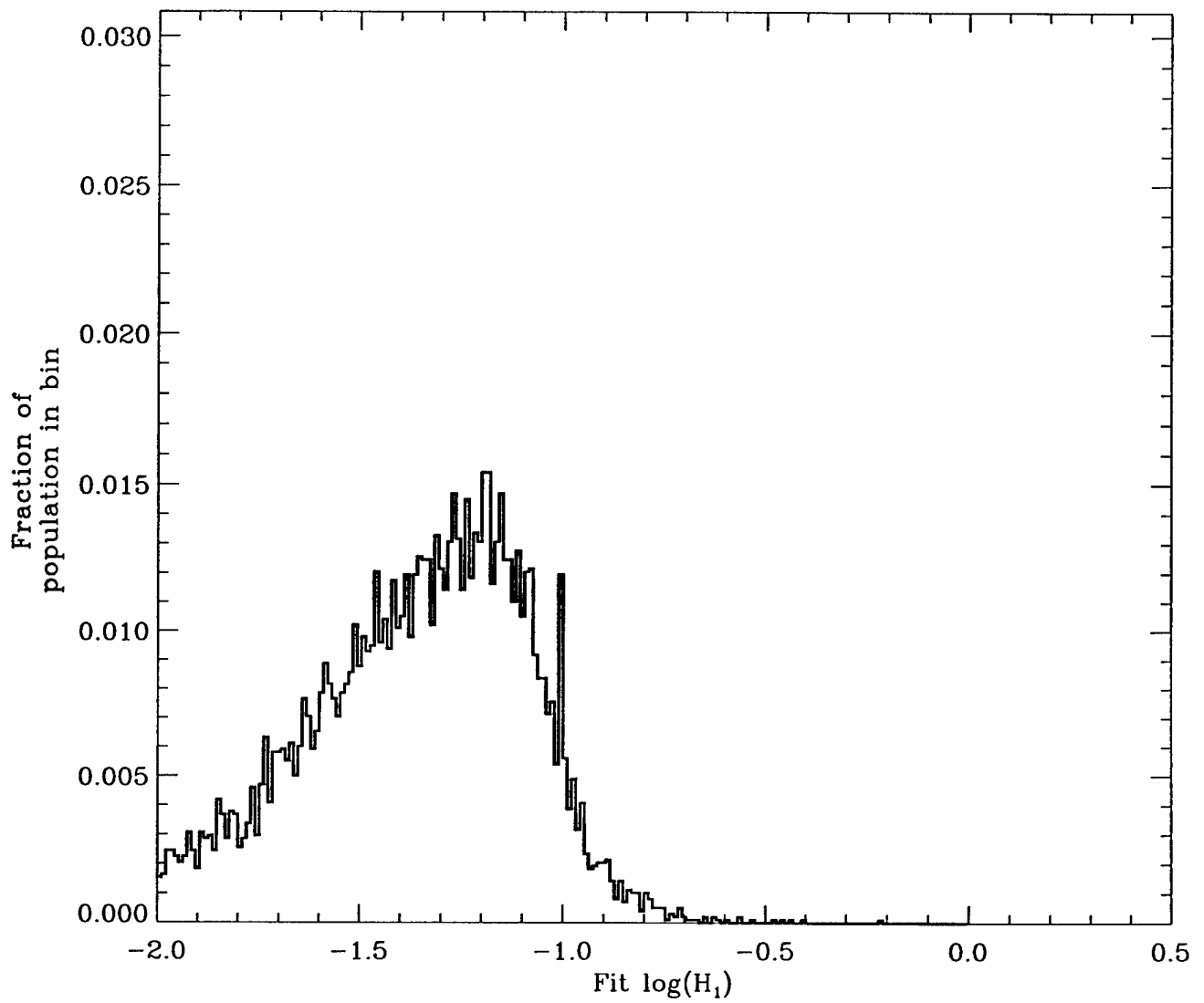
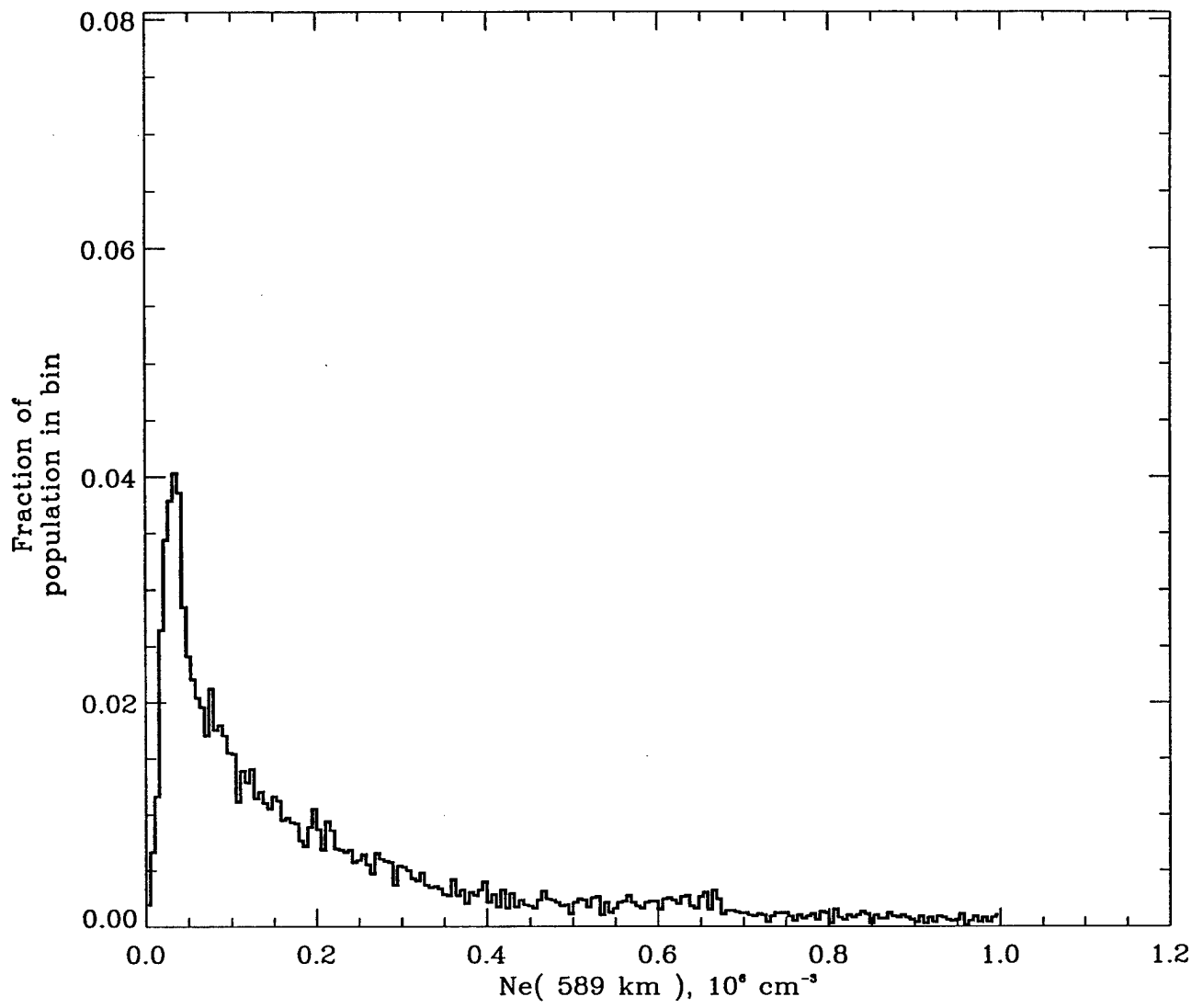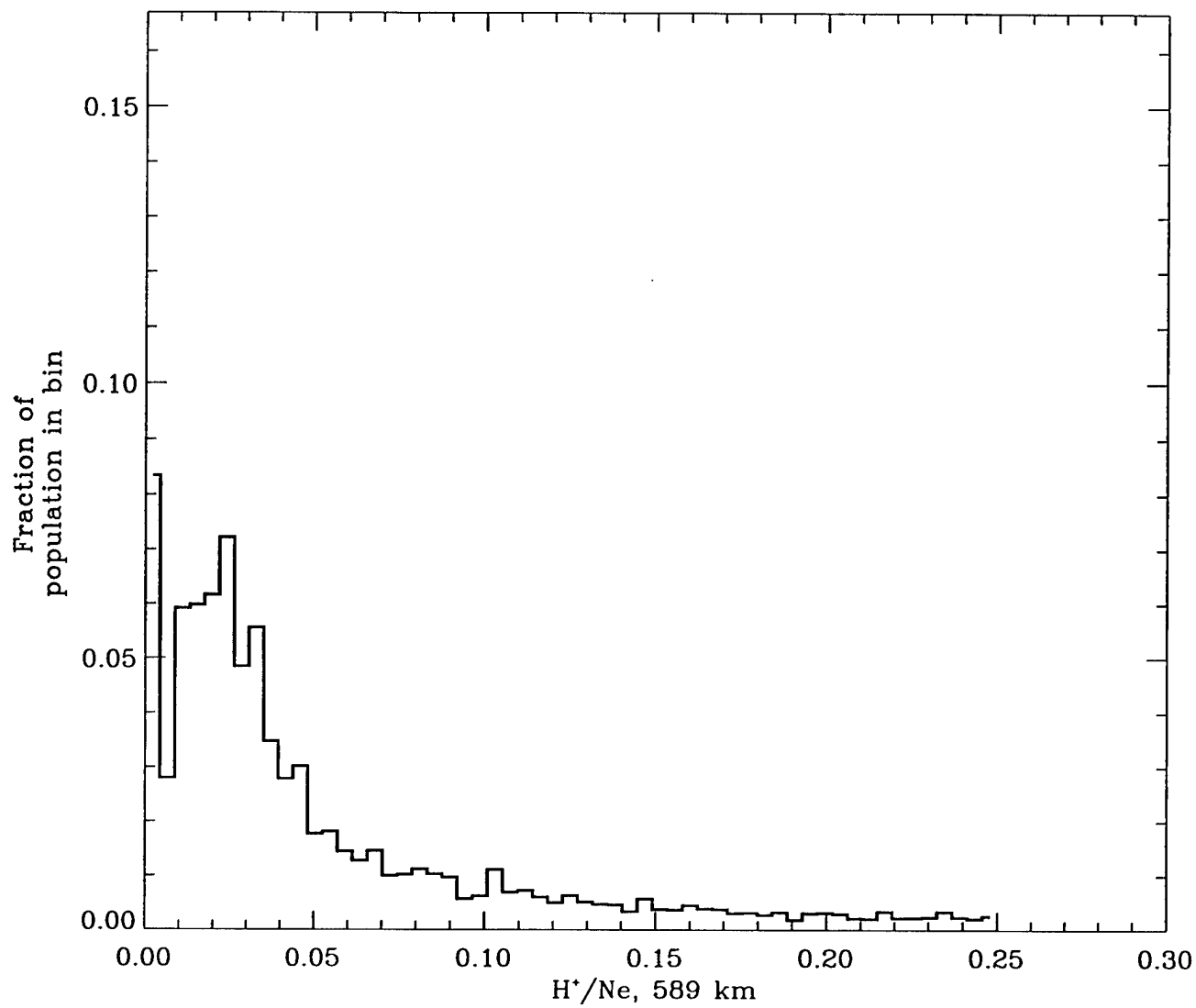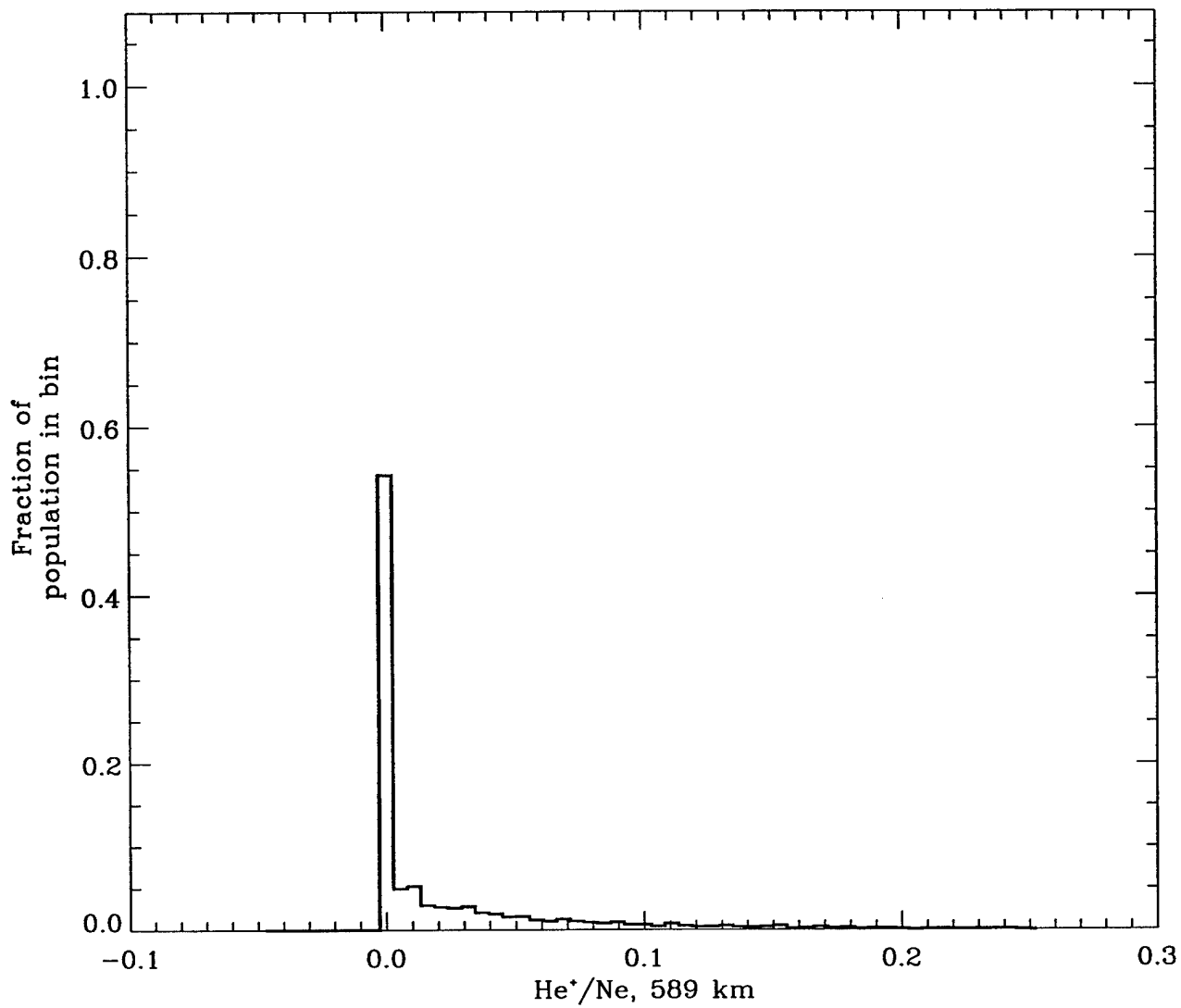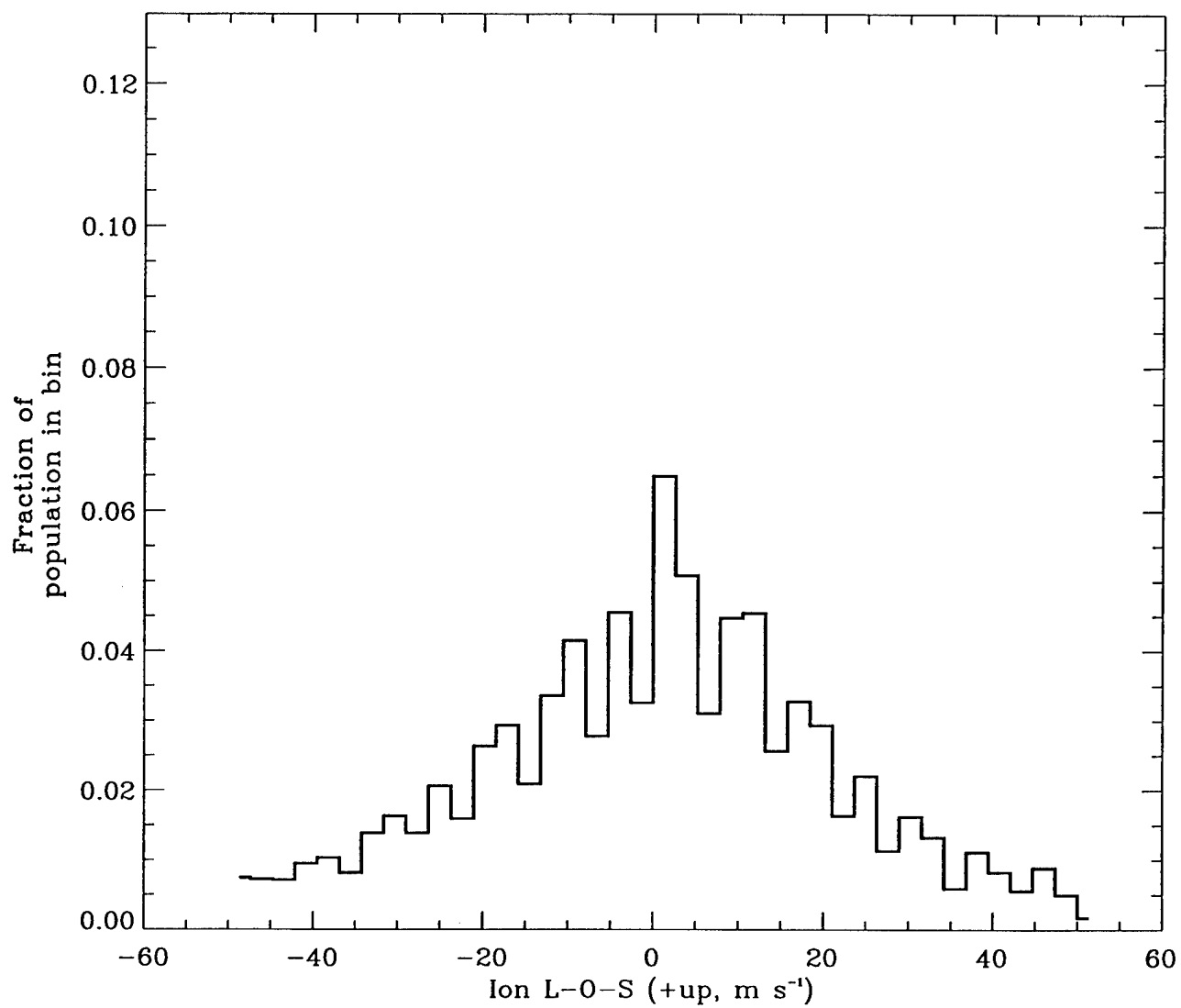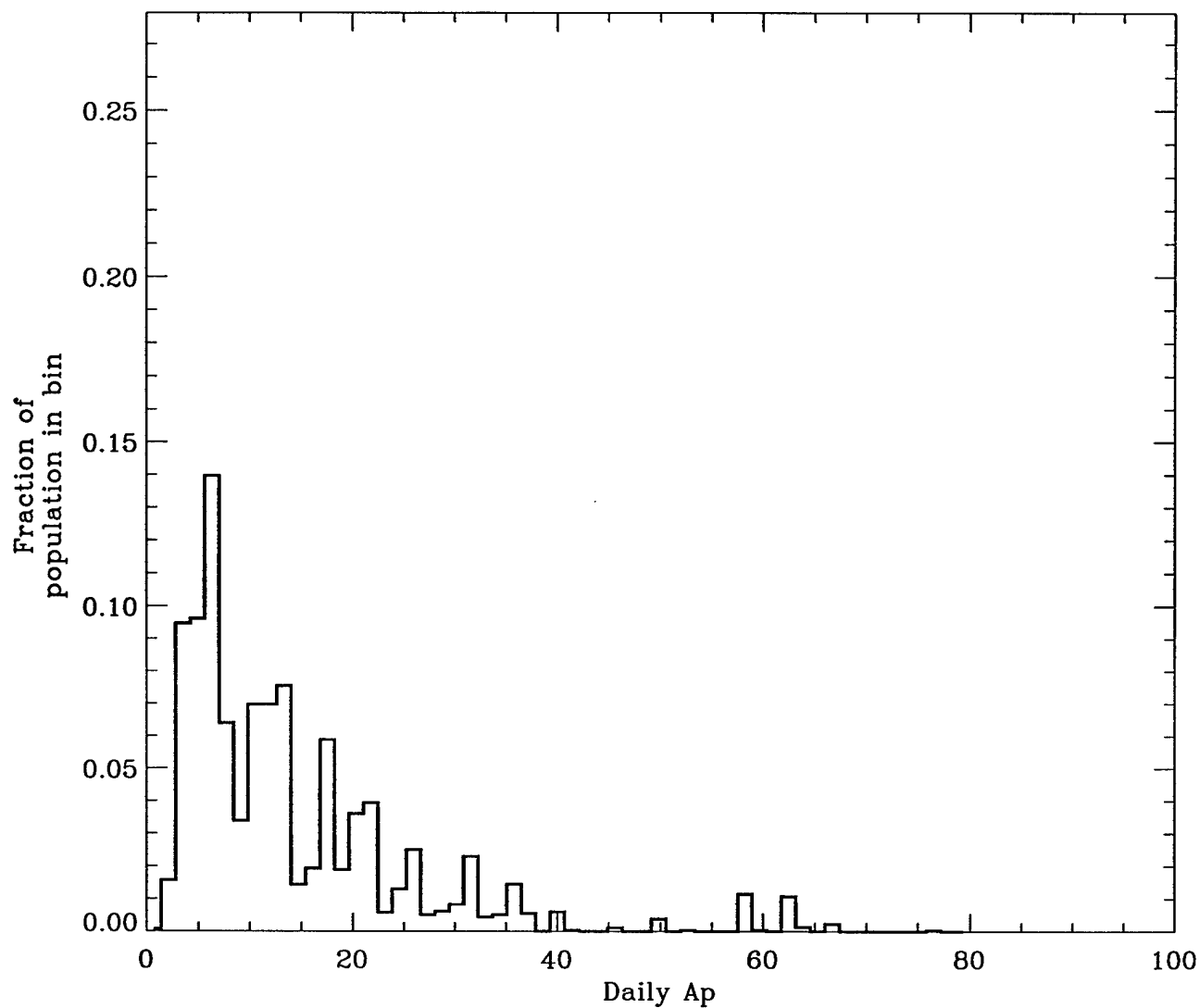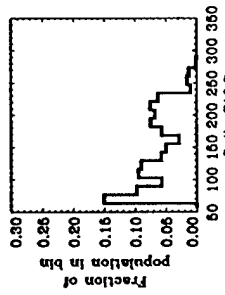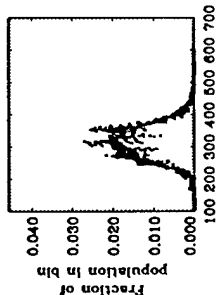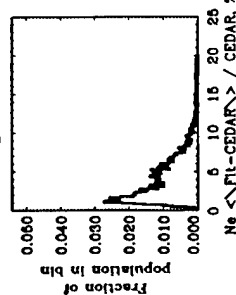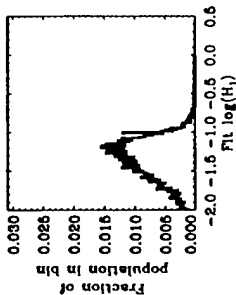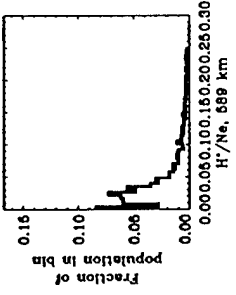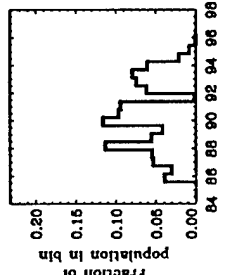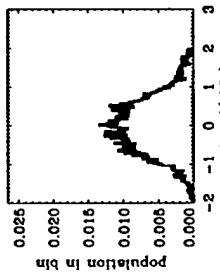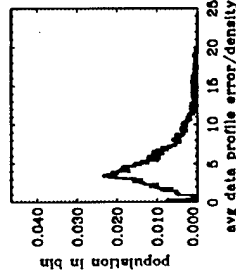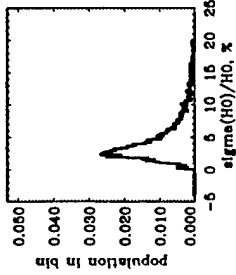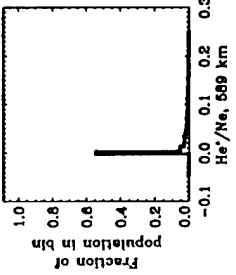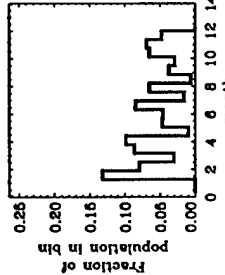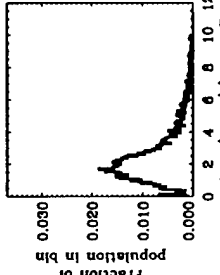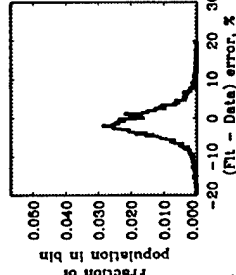Figure-- 19
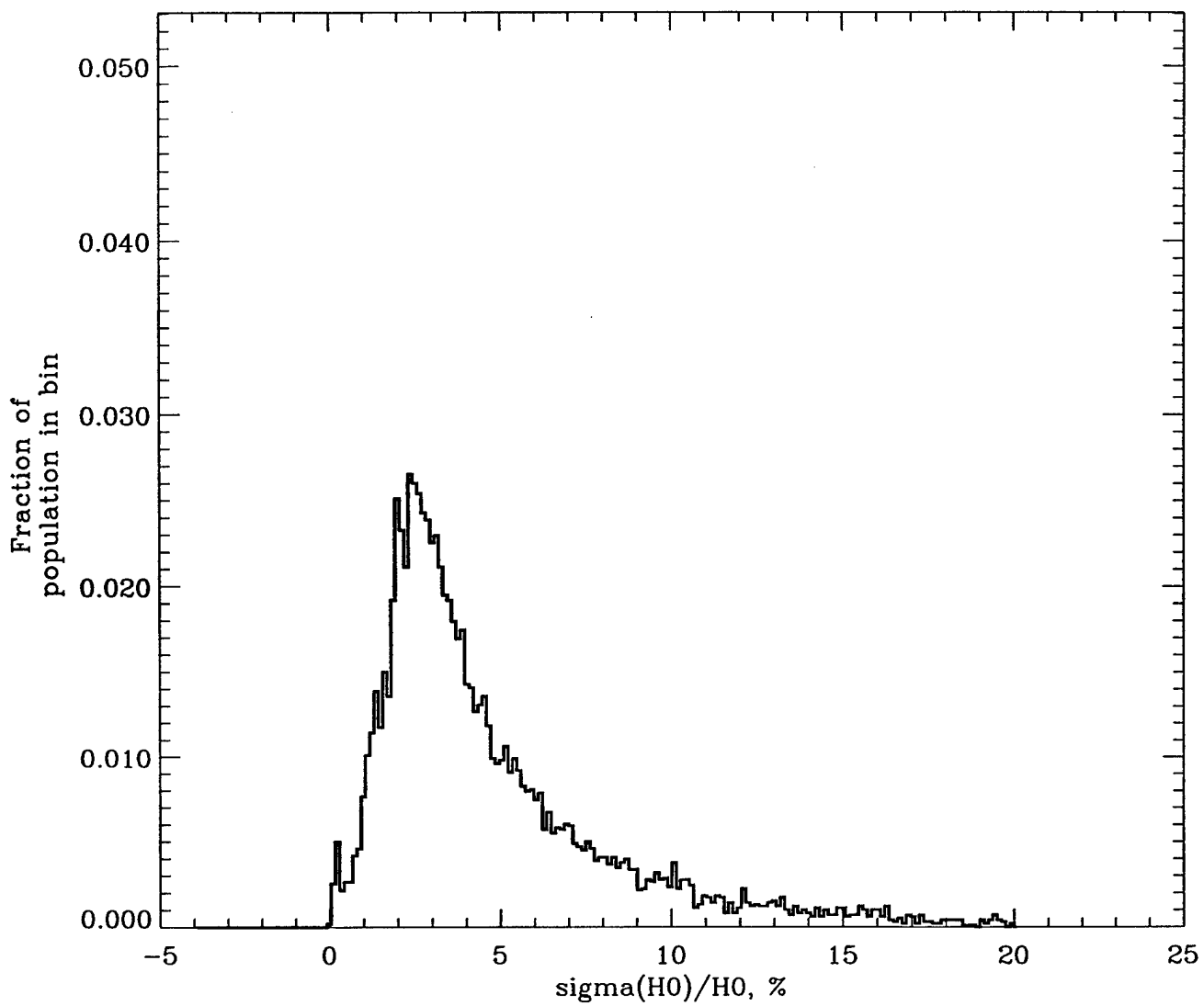
Figure-- 20
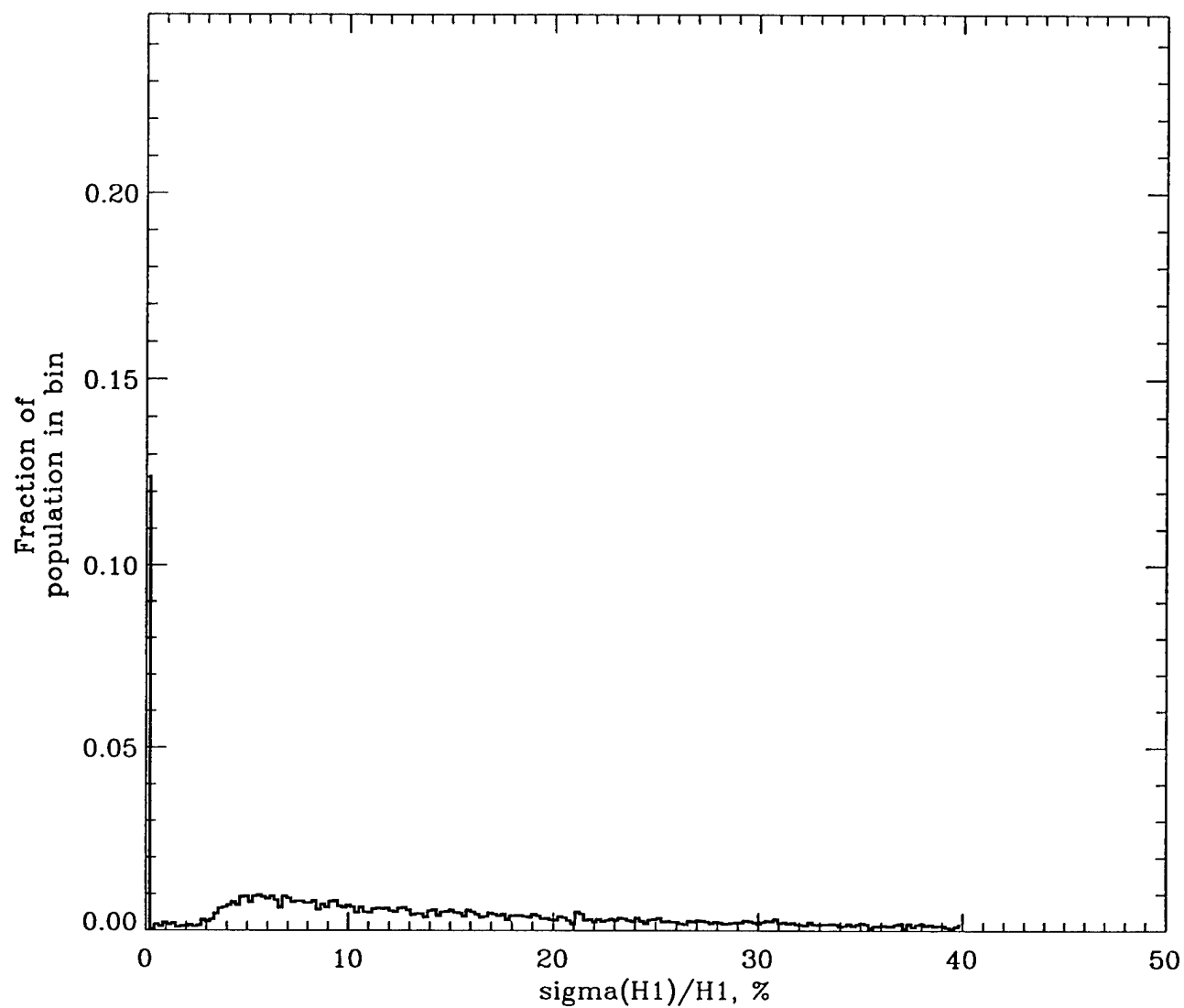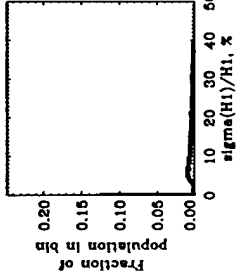
Figure-- 21
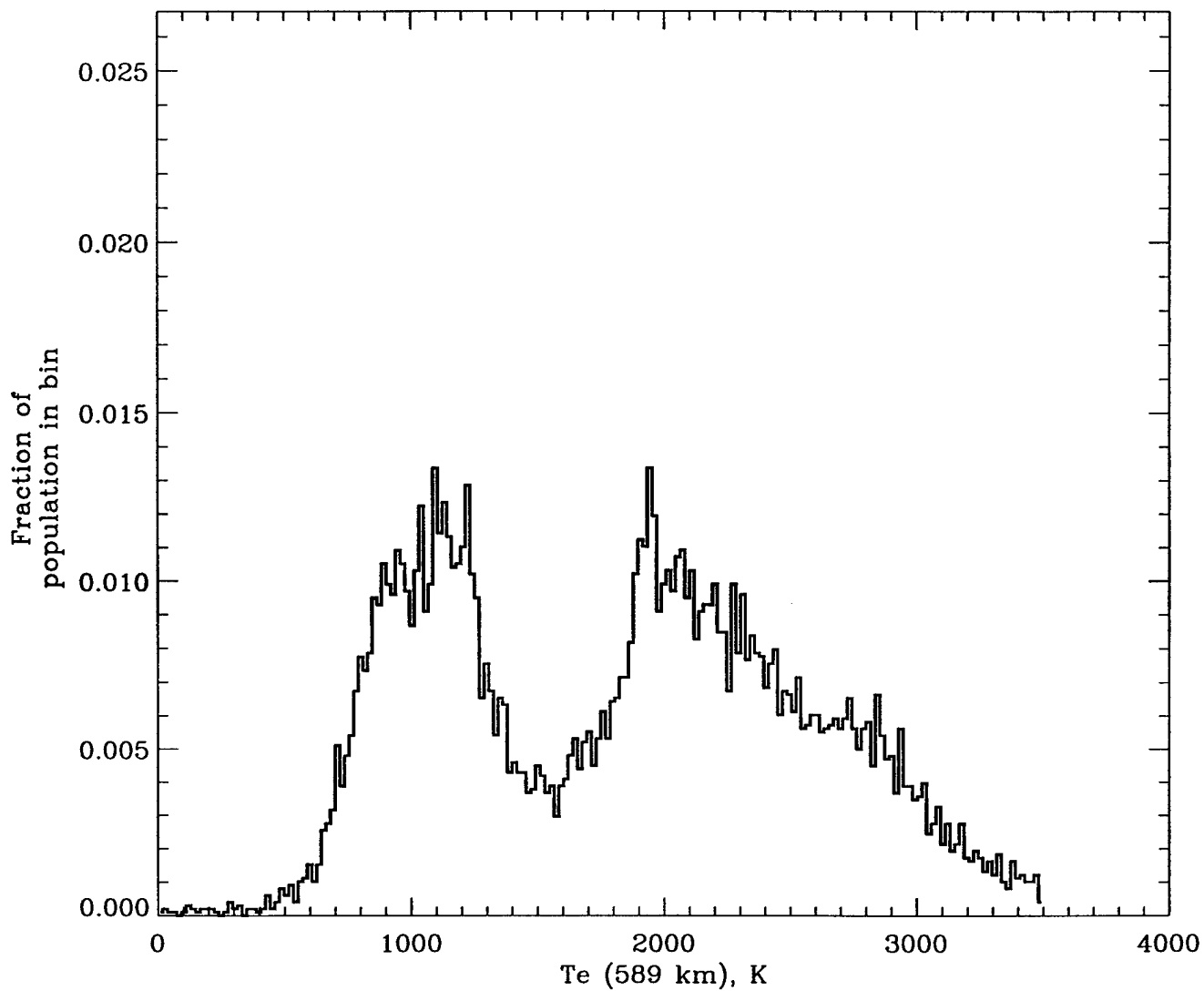
Figure-- 22
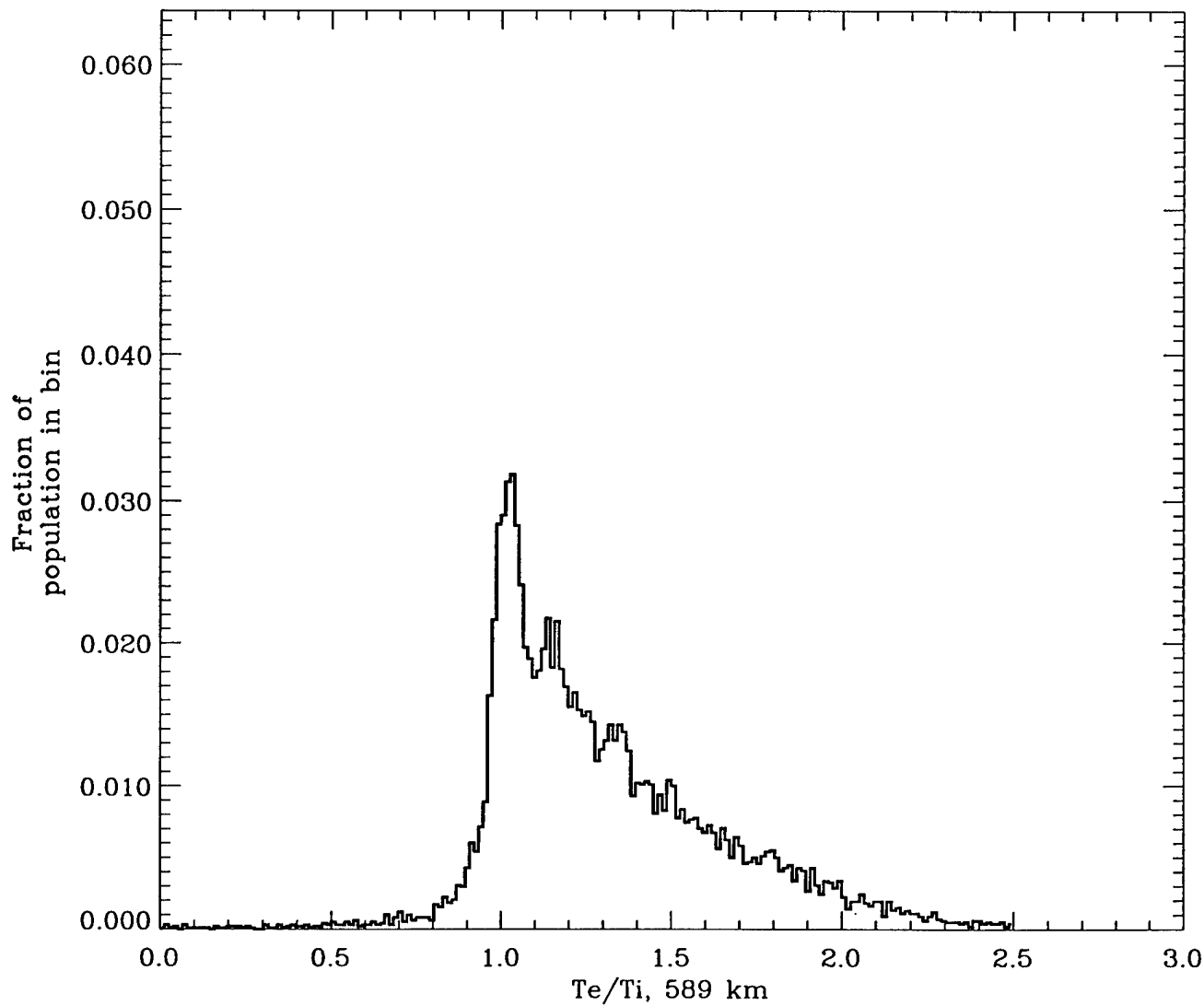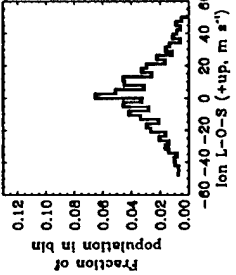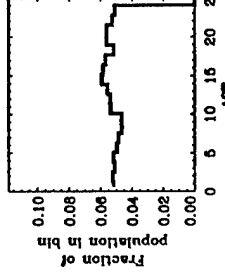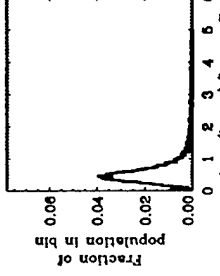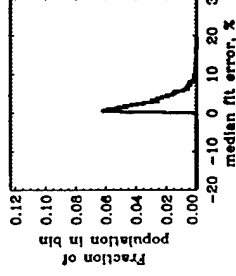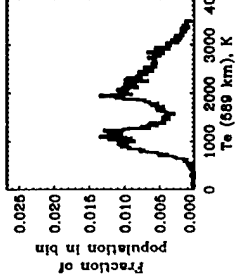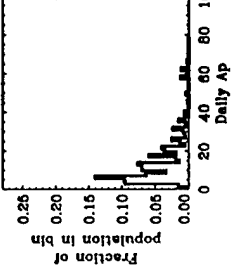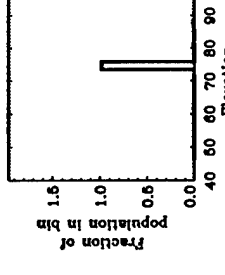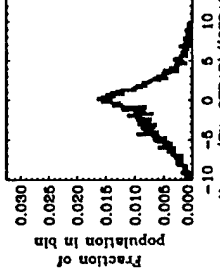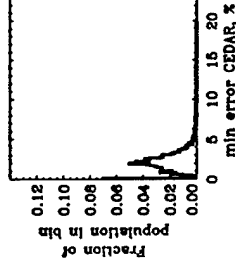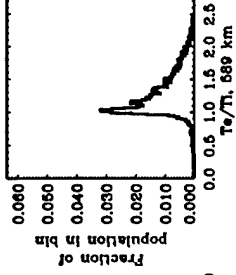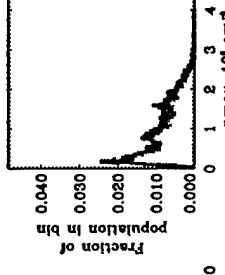
Figure-- 23
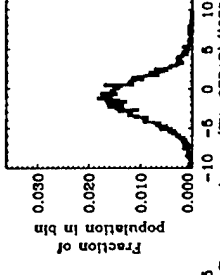
Figure-- 24

Figure-- 25

Figure-- 26

Figure-- 27

Figure-- 28
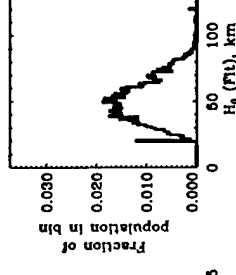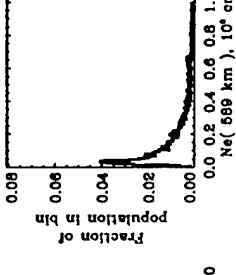
Table 1. Statistical summary of linear-H fits to Arecibo World Days between 1985-1995.

Table 1. (continues) Statistical summary of linear-H fits to Arecibo World Days between 1985-1995

Parameter	Units	Eq	Fig.	Mode	Mode Freq	Mean	σ	Min	Max	Median	Phase of Min (LT)	Phase of Max (LT)	%[B]	Bin Size
F10.7	10^{-22} W m^{-2} Hz^{-1}		1	65-75	0.15	143	57	68	275	133	85-88[A], 94-95[A]	89-92[A]	100	13
Nmax (Fit)	10^5 cm^{-3}		6	2	0.024	9.802	6.7	0.17	40.335	8.514	05-06	13-15	100	0.21
Nmax (CEDAR)	10^5 cm^{-3}		6	2	0.025	7.85203	7.18883	0	43.1	6.03949			100	0.21
hmax (Fit)	km		7	315	0.023	316	51	154	713	316	07-09	22-23	100	2.6
zmax $\neq$ 0 (CEDAR)	km		7	315 350-365	0.028 0.026	320	49	182	686	317	07-09	22-23	82[C]	2.6 2.6
zmax (CEDAR)	km		7	335-360	0.20	262	131	0	686	305	07-09	22-23	100[C]	2.6
χ^2			8	1	0.11	1.14	6.09	0.0001	537253	1.04	23-0130	11-15	100	$\geq$0.16
$\chi^2 \in [0.01,100]$				1	0.12	1.04	4.93	0.01	100	1.007	23-0130	11-15	98	$\geq$0.16
$\chi^2 \in [0.1,10]$				1		1.15	3.27	0.1	10	0.97	23-0130	11-15	84	$\geq$0.16
σ(nmax) / nmax	%	(2)	9	1.75	0.018	35 x 10^6	19 x 10^8	0.002	165 x 10^9	2.4	0530	07-08	100	0.05
$\leq$10%	%	(2)		1.75		2.5	1.7	0.002	10	2.1	0530	07-08	85	0.05
σ(hmax) / hmax	%	(2)	10	$-$0.5	0.04	69 x 10^6	5 x 10^9	0.003	4 x 10^{11}	0.58	Uniform	Uniform	100	0.03
$\leq$ 10%	%	(2)		$-$0.5		0.8	0.9	0.003	0.53	0.53	Uniform	Uniform	86	0.03
(nmax $-$ Nmax) / Nmax	%	(3)	11	0.	0.017	-0.9	4.5	-20	20	-0.6	12-14	07-10	100	0.105
$\leq \pm$10%	%	(3)		0.		-0.9	3.5	-10	10	-0.56	12-14	07-10	96	0.105

(hmax – zmax)

62

Table 1. (continues) Statistical summary of linear-H fits to Arecibo World Days between 1985-1995

Parameter	units	(ref)	#											2	
/ zmax	%		12	-1	0.018	-1.35	3.4	-22.2	24.5	-1.2	10-11	00-01	100	0.105
$B=\langle(n_e-N_e)/N_e\rangle$	%	(3)	13	1	0.027	5	23	0.01	2092	3.6	0030, 1830	11-15	100	0.105
≤ 20%	%	(4)		1		4	3	0.01	20	3.5	0030, 1830	11-1430	98.6	0.105
$D=\langle\sigma(N_e)/N_e\rangle$	%	(4)	14	3	0.024	146047	2×10^6	0.2	92×10^6	4.6	12-1830	03-05	100	0.105
≤ 20%	%	(5)		3		5.4	3.3	0.2	20	4.5	12-1830	03-05	98.1	0.105
$[B-D] \leq \pm100\%$	%	(5)	15	-2	0.029	-1.14	5.6	-100	100	-1.4	06-07	12-16	99	0.21
≤ ± 20%	%	(4)-(5)		-2		-1.23	4.2	-20	20	-1.35	00-01	12-16	98	0.21
Median[|n_e-N_e|/N_e] = F	%	(4)-(5)	16	0.5	0.06	3.4	22	0.00	1493	2.13	00-01	10-11	100	0.21
≤ 20%	%	(6)		0.5	0.06	2.7	2.3	0.00	20	2.12	00-01	10-11	99.5	0.21
$Min[\sigma(N_e)/n_e]$	%	(6)	17	<0.1	0.07	2.2	1.5	10^{-6}	28	2.08	05-06	06-07	100	0.105
≤ 10%	%	(7)		<0.1	0.07	2.2	1.3	10^{-6}	10	2.08	05-06	06-07	99.7	0.105
H_0	km	(7)	18	≈ 50	0.019	51	16	20	120	50	07	14-17, 04,20	100	0.68
$\log H_1$		(1b)	19	-1.2	0.016	-1.7	0.9	-4	-0.22	-1.41	13,2030	06-08	100	0.01
H_1	km / km	(1b)		0.06		0.04	0.03	0.0001	0.6	0.04	13,2030	06-08	100	
$\sigma(H_0)/H_0 \leq$	%	(1b)	20	2.5 / 2.5	0.027	4.5×10^9 / 4.7	4.5×10^{11} / 3.4	0.0008 / 0.0008	4.5×10^{13} / 20	4.14 / 3.6	Uniform / Uniform	Uniform / Uniform	100 / 86.5	0.13
			2											

63

Table 1. Statistical summary of linear-H fits to Arecibo World Days between 1985-1995

	Units	No.	Ref		2.5	5	4.6	0.0008	100	3.6	Uniform	Uniform	3	
20% / $\leq$100%	%, %			0.12	<1	4×10^{11}	3×10^{13}	0.00	2×10^{15}	14	06-10	20-22	87.5	0.21
$\sigma(H_1)/H_1$	%	21		0.013	<1								100	
$\leq$20%	%			0.013	<1	8	6	0.00	20	8	06-10	20-22	62	
$\leq$40%	%			0.013	<1	13	10	0.00	40	11	06-10	20-22	82	
$\leq$100%	%			0.013	<1	19	19.5	0.00	100	13	06-10	20-22	95	
T_e (589 km)	K	22			1100, 1950	1843	747	8	8469	1902	23-05	06-07	100	18.4
$\leq$4000 K	K				1100, 1950	1836	732	8	4000	1901	23-05	06-07	99.7	18.4
T_e/T_i (589 km)		23		0.032	1.03	1.3	0.41	0.005	18	1.224	20-03	06-07	100	0.013
$\geq$1.0					1.0	1.4	0.40	1.000	18	1.283	20-03	06-07	86.8	
$\in[1,3]$					1.0	1.37	0.32	1.00	3	1.282	20-03	06-07	86.6	
Ne (589 km)	10^5 cm^{-3}	24	(1)	0.04	0.3	2.29	2.5	0.01	38.3	1.33			100	0.05
H$^+$ (589 km)	H$^+$/Ne, %	25		0.08	<1, 2.5	13	21	0.00	720	3.9	09-18	02-04	100	4.4
$\leq$100%	H$^+$/Ne, %			0.08	<1, 2.5	12.5	19	0.00	100	3.9	09-18	02-04	99.7	
He$^+$ (589 km)	He$^+$/Ne, %	26		0.55	$\approx$0	3	9	0.00	534	0	09-22	03,05-06	100	0.53
$\leq$100%	He$^+$/Ne, %			0.55	$\approx$0	3	6	0.00	100	0	09-22	03,05-06	99.9	0.53
V_r (589 km)	m s^{-1}	27	(7)-(9)	0.033	0	-4.3	336	-32767	971	0	19-20[D]	06-07	100	1.2
$\leq\pm$60	m s^{-1}		(7)-(9)		0	0.3	23	-60	60	0	19-20[D]	06-07	87.8	1.2
$\leq\pm$100	m s^{-1}		(7)-(9)		0	-0.08	31	-100	100	0	19-20[D]	06-07	94.7	1.2
Ap		28		0.16	4 – 8	14	12	1	76	11	Uniform	Uniform	100	1.2

* A = year, B = sample of 9801 fits, C=sample of 14000 profiles, D=downward maximum, σ = standard deviation of sample.